

Holographic Floquet states in low dimensions (II)

Martí Berenguer, Ana Garbayo, Javier Mas and Alfonso V. Ramallo

*Departamento de Física de Partículas, Universidade de Santiago de Compostela, and
Instituto Galego de Física de Altas Enerxías (IGFAE),
E-15782 Santiago de Compostela, Spain*

E-mail: marti.berenguer.mimo@usc.es, ana.garbayo.peon@usc.es,
javier.mas@usc.es, alfonso@fpaxp1.usc.es

ABSTRACT: We continue the study in [1] of a strongly coupled (2+1)-dimensional gauge theory subject to an external rotating electric field. The system is modelled holographically as a D3/D5 probe intersection. We add temperature to the D3 background and analyze the phase diagram. Also here, the conductive phase extends down to vanishing external electric field at discrete values of the frequencies where *vector meson Floquet condensates* form. For all temperatures, at given intercalated frequencies, we find new dual states that we name *Floquet suppression points* where the vacuum polarization vanishes even in the presence of an electric field. From the data we infer that these states exist both in the conductive and insulating phases. In the massless limit we find a linear and instantaneous conductivity law, recovering known general results in 2+1 dimensions. We also examine the photovoltaic AC and DC current as the response to an oscillating probe electric field and see that rising the temperature suppresses the photovoltaic Hall current. All the results obtained carry over qualitatively unaltered to the case of D3/D7.

KEYWORDS: AdS-CFT Correspondence, D-Branes, Gauge-Gravity Correspondence

ARXIV EPRINT: [2209.03884](https://arxiv.org/abs/2209.03884)

Contents

| | | |
|----------|---|-----------|
| 1 | Introduction and conclusions | 1 |
| 2 | D3/D5 system at finite temperature | 3 |
| 3 | Phase space | 7 |
| 3.1 | Floquet suppression points | 12 |
| 4 | Non-linear conductivity | 13 |
| 5 | Photovoltaic optical conductivity | 16 |
| 6 | Summary and outlook | 18 |
| A | Coordinates and D5-brane action | 20 |
| B | Holographic dictionary | 23 |
| C | Effective horizon and effective temperature | 25 |
| D | Analytic solutions | 27 |
| D.1 | Massless solution | 27 |
| D.2 | Small mass solutions | 30 |
| E | Photovoltaic conductivities | 32 |
| E.1 | Massless limit | 34 |
| F | Linearized Minkowski embeddings and meson spectrum | 36 |
| G | Phase space structure for the D3/D7 system | 38 |

1 Introduction and conclusions

Periodically driven systems form a separate chapter in the book of non equilibrium dynamics. Much progress has been achieved both at theoretical and experimental level in the path to control their effective long time dynamics [2–8]. This has opened the way to engineer Hamiltonians that embody non trivial phenomena and new phases of quantum materials. Of particular interest is the case of solutions where energy injection and dissipation balance, thereby reaching a Floquet type of *non-equilibrium steady state* (NESS). In a series of previous papers, the existence of a Floquet NESS has been studied in the context of the AdS/CFT correspondence both in the case of a D3/D7 system [9, 10], and of a D3/D5

system [1]. In these intersections the higher dimensional flavor brane is treated as a probe in the background of a $AdS_5 \times S^5$ geometry. The flavor degrees of freedom experience the rotating external field, while they are coupled to the non abelian “gluon” vacuum acting as a bath. The crucial ingredient that allows for the system to be solved numerically is the fact that, in the rotating frame, the action becomes time independent and, therefore, all differential equations turn out to be of the ordinary type. This is a remarkable ansatz where the technique developed in [11] can still be applied to obtain the fully non-linear one point functions just from demanding reality of the action. In the literature, this extremely useful IR fixing mechanism has been applied to several static configurations. For time dependent sources very little is known. In spatial dimension $d_s = 2$, and for massless charge carriers, the current response is linear and instantaneous $j(t) = \sigma E(t)$ [12]. Our results are consistent with this observation in the limit of small mass flavours.

In this paper we deal with the D3/D5 system, in which the D3- and D5-branes share two spatial directions. The field theory dual to this brane setup is well-known and consists of a supersymmetric theory with flavor hypermultiplets living in a two-dimensional defect coupled to an ambient $\mathcal{N} = 4$ four-dimensional Yang-Mills theory [13–15]. In this work, which is a continuation of [1], we add a background temperature to the adjoint degrees of freedom which, therefore, are now deconfined. The nonzero temperature breaks supersymmetry and adds charged carriers to the ones previously formed by Schwinger pair production. These are naturally melted mesons that are present at finite temperature for low enough quark mass. Therefore, the phenomenology is expected to yield a continuous deformation of the case at zero temperature.

It is known that the fluctuations of the flavor brane degrees of freedom feel another temperature, T_{eff} , through an effective metric named *open string metric*. That this is a *bona fide* temperature has been the subject of careful studies that examined, for example, the universality of the fluctuation dissipation relations [16]. In most common cases the effective temperature is larger than the bulk temperature of the gluon plasma $T_{\text{eff}} > T$. Some exceptional cases have been reported where the inequality is reversed [17]. We don’t find such exceptional situation after scanning throughout our phase space.

The plan of the paper is the following. In section 2 we shall set up the stage and the notation although most of the details are relegated to appendix A. The phase space is examined in section 3. Section 4 is devoted to a detailed study of the macroscopic rotating current generated in response to the rotating electric field. In particular, the relative angle between them shows an interesting pattern as a function of the driving frequency Ω . Section 5 is devoted to the study of the so called photovoltaic current, namely the response of the Floquet NESS to an additional AC electric field that probes the modified conduction properties of the medium as a result of the rotating electric field applied. In section 6 we summarize our results and discuss some possible extensions of our work.

The paper is completed with some appendices containing many details and explicit calculations which might be useful for the interested reader. In appendix A we collect the different systems of coordinates used and the expression of the corresponding D5-brane action. In appendix B we work out the holographic dictionary for our system. In appendix C we analyze the effective horizon and temperature of the Floquet system.

Appendix D is devoted to the analytic solutions of the equations of motion with zero and small quark mass, and we check explicitly the consistency of the holographic dictionary developed in appendix B for this particular case. In appendix E we review the general formalism to compute the photovoltaic conductivities, which we obtain analytically in the massless limit at non-vanishing temperature. In appendix F we study the linearized Minkowski embeddings and the calculation of the mesonic spectra at non-zero temperature. Finally and for completeness, in appendix G we include the phase space for the D3/D7 system.

In what respects the addition of a background temperature, the take home message is that it acts in the same direction as an increase in the module of the electric field. Hence, many delicate phenomena related to the vicinity to critical embeddings get screened away.

2 D3/D5 system at finite temperature

In this section we will set up the stage and review the main results obtained in this study for the D3/D5 systems. We chose to parametrize the D5 brane embeddings with an angular coordinate function $\psi(u) \in [0, 1]$ where $\psi(u) = 0$ corresponds to massless embeddings and the boundary of AdS sits at $u = \infty$. The induced metric takes the form

$$ds^2 = g_{tt}dt^2 + g_{ii}(dx^2 + dy^2) + g_{uu}du^2 + g_{\Omega\Omega}d\Omega_2^2 \quad (2.1)$$

where $d\Omega_2^2$ is the metric of a unit two-sphere and

$$g_{tt} = -\frac{u^2}{R^2} \frac{g^2(u)}{h(u)}, \quad g_{ii} = \frac{u^2}{R^2} h(u), \quad g_{uu} = R^2 \left(\frac{1}{u^2} + \frac{\psi'^2}{1-\psi^2} \right), \quad g_{\Omega\Omega} = R^2(1-\psi^2)$$

with

$$g(u) = 1 - \frac{u_h^4}{u^4}, \quad h(u) = 1 + \frac{u_h^4}{u^4} \quad (2.2)$$

This black hole metric has a Hawking temperature

$$T = \frac{\sqrt{2} u_h}{\pi R^2} = \frac{r_h}{\pi R^2}. \quad (2.3)$$

where we have written T both in terms of the isotropic coordinate u and the cartesian coordinate r related by (A.5). At the horizon there is merely a factor $r_h = \sqrt{2} u_h$ among them (in what follows we will take $R = 1$). In the remaining we will parametrize background temperatures in terms of r_h/m .

We want to study the response of these systems to an external driving by a circularly polarized electric field

$$\vec{\mathcal{E}}(t) = \begin{pmatrix} \mathcal{E}_x(t) \\ \mathcal{E}_y(t) \end{pmatrix} = \begin{pmatrix} \cos \Omega t & -\sin \Omega t \\ \sin \Omega t & \cos \Omega t \end{pmatrix} \begin{pmatrix} E_x \\ E_y \end{pmatrix} \equiv O(t) \vec{E}, \quad (2.4)$$

with $\vec{E} = \vec{\mathcal{E}}(t=0)$. To properly account for the rotation it is convenient to complexify this field $\mathcal{E}(t) = \mathcal{E}_x(t) + i\mathcal{E}_y(t)$

$$\mathcal{E}(t) = E e^{i\Omega t} = -i\Omega A e^{i\Omega t} \quad (2.5)$$

where A is the boundary value of a world-volume gauge field one-form

$$2\pi \alpha' \mathcal{A}(t, u) = a_x(t, u) dx + a_y(t, u) dy, \quad (2.6)$$

The Born Infeld action reduces to

$$\frac{I_{D5}}{\mathcal{N}} = - \int du g_{\Omega\Omega} \sqrt{g_{ii}^2 |g_{tt}| g_{uu} - (\text{Im}(\bar{a}'\dot{a}))^2 + g_{ii}(|g_{tt}| |a'|^2 - g_{uu} |\dot{a}|^2)} \quad (2.7)$$

with $\mathcal{N} \equiv 4\pi N_f T_{D5} \text{vol}(\mathbb{R}^{1,2})$. The complexification in (2.5) motivates to do it also at the level of the bulk fields

$$a(t, u) = a_x(t, u) + i a_y(t, u) = c(t, u) e^{i\Omega t}, \quad (2.8)$$

leading to the following form of the action¹

$$\frac{I_{D5}}{\mathcal{N}} = - \int du g_{\Omega\Omega} \sqrt{g_{ii}^2 |g_{tt}| g_{uu} - (\text{Im}(\bar{c}'\dot{c}) + \Omega \text{Re}(\bar{c}'\dot{c}))^2 + g_{ii}(|g_{tt}| |c'|^2 - g_{uu} (|\dot{c}|^2 + \Omega^2 |c|^2 + 2\Omega \text{Im}(\dot{c}\bar{c})))}$$

A particular ansatz is to assume that $c(t, u) = c(u)$. Hence $\dot{c} = 0$ and the only remnant of the rotating dynamics is the presence of the parameter Ω . To exhibit the presence of a conserved quantity it is convenient to switch to a polar image with $c(u) = b(u) e^{i\chi(u)}$. Then

$$\frac{I_{D5}}{\mathcal{N}} = - \int du \sqrt{(1 - \psi^2) [(u^4 g^2 - \Omega^2 b^2) ((1 - \psi^2) b'^2 + h(1 - \psi^2 + u^2 \psi'^2)) + (1 - \psi^2) u^4 g^2 b^2 \chi'^2]}$$

and the searched for conserved quantity is the one associated to the shift symmetry of χ

$$q \equiv \Omega \frac{\partial \mathcal{L}}{\partial \chi'}. \quad (2.9)$$

As has become the usual case when there is an electric field switched on [11], demanding reality of the Routhian (partial Legendre transform with respect to χ)

$$\frac{\tilde{I}_{D5}}{\mathcal{N}} = - \int \frac{du}{\Omega b g u^2} \sqrt{(\Omega^2 b^2 - u^4 g^2) (q^2 - u^4 \Omega^2 b^2 g^2 (1 - \psi^2)^2) \left(b^2 + h + \frac{u^2 h \psi'^2}{1 - \psi^2} \right)} \quad (2.10)$$

imposes that the first two terms under the square root must vanish at the same point $u = u_c$, which locates the so called *singular shell*. At once, this condition fixes both the value of u_c and that of the conserved quantity q

$$b_0 = \frac{u_c^4 - u_h^4}{\Omega u_c^2}, \quad q = \frac{(u_c^4 - u_h^4)^2}{u_c^4} (1 - \psi_0^2), \quad (2.11)$$

where $b_0 = b(u_c)$, $\psi_0 = \psi(u_c)$. As $b_0 \geq 0$ we see that $u_c \geq u_h$ and the singular shell sits always at a larger radius than the black hole horizon. Moreover, here it is the IR data b_0 what controls the position of $u_c(u_h, b_0)$. This is unlike the case of constant E [11]. Hence the shape of the critical surface at constant $|E|$ is non spherical, as can be seen in figure 1.

¹Notice that, unlike the case of a constant background electric field $A_x = -Et + \dots$ [11], in this case there is no explicit dependence on the UV value of the source in the action. This is a notorious difference that is at the heart of many differences among the two cases. For example the fact that the critical radius is not only dependent on the value of $|E|$ in our case.

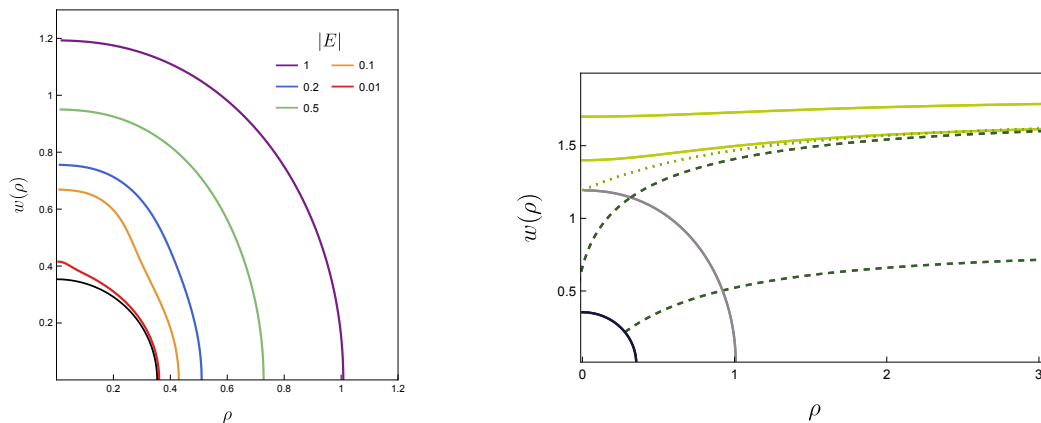


Figure 1. *Left plot:* shapes of the singular shells as a function of the applied electric field. The axes are $\rho = u\sqrt{1 - \psi^2}$ and $w = u\psi$ with $\psi = \sin\theta$. The curves are the points $\rho^2 + w^2 = u_c(E, \psi_0)$ with $\psi_0 = \sin\theta_0$ the embedding angle at the singular shell. Outside the limit $E \rightarrow 0$ the shell shape is non spherical. Hence, unlike the case of a constant electric field, in the rotating situation we have a non trivial dependence of u_c on the mass m of the D5-brane at fixed $|E|$. *Right plot:* profiles of different embeddings for $\Omega = |E| = 1$. The dashed lines represent black hole embeddings. They can be either regular (thermal), ending on the horizon, or singular, ending in a conical singularity. The dotted line represents a critical embedding. The solid lines represent Minkowski embeddings. The black hole and pseudo-horizon are shown by the black (inner) and gray (outer) lines.

There are three types of embeddings in place now. First of all, we find the *Minkowski* embeddings, which do not intersect the singular shell. They end up closing smoothly at a value of $u = u_0$ while $\psi = 1$. With *black hole* (BH) embeddings we will generically denote solutions that intersect the singular shell. This accounts for the fact that for a world-volume observer the singular shell acts as an event horizon, inducing thermal effects through Schwinger pair production. For this reason, we will term interchangeably singular shell and effective horizon.

Black hole embeddings can be further subdivided into two classes, *thermal* and *conical*. The first ones hit the bulk black hole horizon, while the second ones close up at $\psi = 1$ with a conical singularity, most likely a reflection of the sink of energy pumped by the electric field in a conducting albeit non-dissipative system. These conical black hole embeddings are the remnant of the ones that were studied in [1] at zero temperature. For a constant electric field they were analyzed in [18, 19].

As a technical remark, notice that, in order to solve numerically for the black hole embeddings, boundary conditions must be placed at the singular shell. The first derivatives are then not free but commanded by regularity (see eqs. (A.16), (A.17) and (A.18)). In contrast, we could place boundary conditions at the background horizon for the embedding function ψ and the module b , but not for the phase χ since this function diverges logarithmically as $\log(u - u_h)$ (see eq. (A.21)). Starting from the effective horizon, then, one can integrate either outwards or inwards and this is how the thermal and/or conical embeddings are completed.

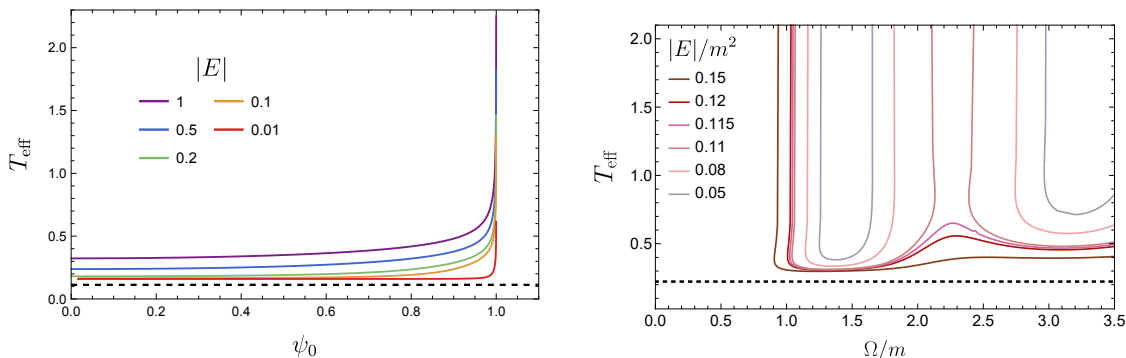


Figure 2. *Left plot:* effective temperature for different BH embeddings labelled by the insertion angle at the effective horizon $\psi_0 = \psi(u_c)$. *Right plot:* effective temperature as we vary Ω/m at fixed $|E|/m^2$. In both cases, the divergence in T_{eff} arises as the curves come close to the critical embeddings. In both plots, the lowest dashed line in black signals the background temperature.

As mentioned before, and explained in appendix C, the critical radius u_c signals the position of an event horizon in the induced open string metric which governs the dynamics of the worldsheet fluctuations. Associated with it, we find an effective temperature

$$T_{\text{eff}} = \frac{2u_c h(u_c) - \Omega b'(u_c)}{2\pi b(u_c) \chi'(u_c)}. \quad (2.12)$$

As in the vast majority of the situations encountered in the literature, here we also find that $T_{\text{eff}} > T$ as far as we have been able to scan, as shown in figure 2.

As usual, the UV asymptotic analysis establishes the holographic dictionary. Near the UV boundary $u \rightarrow \infty$, the fields $\psi(u)$, $b(u)$, $\chi(u)$ behave as

$$\psi(u) = \frac{m}{u} + \frac{\mathcal{C}}{u^2} + \dots \quad (2.13)$$

$$c(u) = A + \frac{j}{u} + \dots = b(u) e^{i\chi(u)}, \quad (2.14)$$

with $A = iE/\Omega$. From where we can read off the 1-point functions \mathcal{C} and j for the chiral condensate and the electric current respectively.

The relation between E , j , m and \mathcal{C} and the electric field $\mathcal{E}_{\text{YM}}(t)$, the electric current $\mathcal{J}_{\text{YM}}(t)$, quark mass m_q and quark condensate $\langle O_m \rangle$ in the boundary theory are

$$\mathcal{E}_{\text{YM}}(t) = \sqrt{\frac{\lambda}{2\pi^2}} e^{i\Omega t} E, \quad \mathcal{J}_{\text{YM}}(t) = \frac{N_f N_c}{\pi^2} e^{i\Omega t} j, \quad (2.15)$$

$$m_q = \sqrt{\frac{\lambda}{2\pi^2}} m, \quad \langle O_m \rangle = -\frac{N_f N_c}{\pi^2} \mathcal{C}, \quad (2.16)$$

where $\lambda = g_{\text{YM}}^2 N_c$ is the 't Hooft coupling of the $\mathcal{N} = 4$ theory. Using this asymptotics, the integration constant in (2.11) acquires the meaning of a Joule heating

$$q = \frac{\Omega \rho^4}{\mathcal{L}} \text{Im}(\bar{c} c') = \vec{j} \cdot \vec{E}. \quad (2.17)$$

Only black hole embeddings have a non zero value for this quantity. The stationarity of the background metric upon this energy injection can only be understood as a transient effect due to the imbalance $N_f/N_c \sim 0$ that is present in the probe limit. In the presence of a black hole in the bulk, the long time effect of a non-negligible backreaction would be a slow increase in the horizon radius.

An important remark for later use is the fact that both the worldvolume electric field and the black hole horizon add up their effects of bending the brane in the IR towards the origin $r \rightarrow 0$. This will mean that as we increase the temperature we will find black hole embeddings with milder electric fields.

The following is a scaling symmetry of the lagrangian $\mathcal{L} \rightarrow \alpha^2 \mathcal{L}$ and the boundary conditions

$$\begin{aligned}
 t &\rightarrow t/\alpha, & u &\rightarrow \alpha u, & w &\rightarrow \alpha w, & b &\rightarrow \alpha b, & \chi &\rightarrow \chi, \\
 \Omega &\rightarrow \alpha \Omega, & E &\rightarrow \alpha^2 E, & j &\rightarrow \alpha^2 j, & \psi &\rightarrow \psi, & & \\
 m &\rightarrow \alpha m, & \mathcal{C} &\rightarrow \alpha^2 \mathcal{C}, & q &\rightarrow \alpha^4 q, & T &\rightarrow \alpha T, & T_{\text{eff}} &\rightarrow \alpha T_{\text{eff}}.
 \end{aligned}
 \tag{2.18}$$

By choosing $\alpha = 1/m$ in (2.18) we can make $m = 1$ and deal with the remaining quantities in units of (the appropriate powers of) m .

3 Phase space

The standard lore in flavor branes is that Minkowski (black hole) embeddings are dual to insulating (conducting) phases of the quantum system. In the case of a rotating electric field, we must be more careful. Actually, two types of currents emerge. Black hole embeddings carry dissipating currents because of the presence of fundamental carriers. The external driving has to supply energy in order to maintain the stationary rotating current.

For Minkowski embeddings j is a polarization current. In analogy with the case of D3/D7 [10], we interpret this polarization as a coherent alignment of the vector meson vacuum fluctuations parallel to the electric field. The polarization current is the time derivative of the polarization and rotates at right angles with the electric field, signalling zero Joule heating, hence not dissipating any energy. This conservative aspect allows for the possibility to have non-zero persistent current even in the limit of vanishing driving field. As we will see, there exists a dual possibility, namely, the dynamical cancellation of the polarizability of the vacuum at discrete frequencies.

In figure 3 we show how the background temperature affects the splitting of the phase space into the two types of embeddings. For a given temperature, points on the corresponding curve represent critical embeddings, pictured in dashed black on the right plot in figure 1. Roughly speaking, points above such curves correspond to black hole embeddings, whereas those below are Minkowski. However, close to the lines, the situation can be multivalued and we can find both types of embeddings in the near vicinity. The lobed structure was already present at zero temperature [1, 10].

We can observe that the effect of increasing the temperature is a depletion of the height of the lobes with rising r_h , until they fully disappear beyond some temperature. Let us

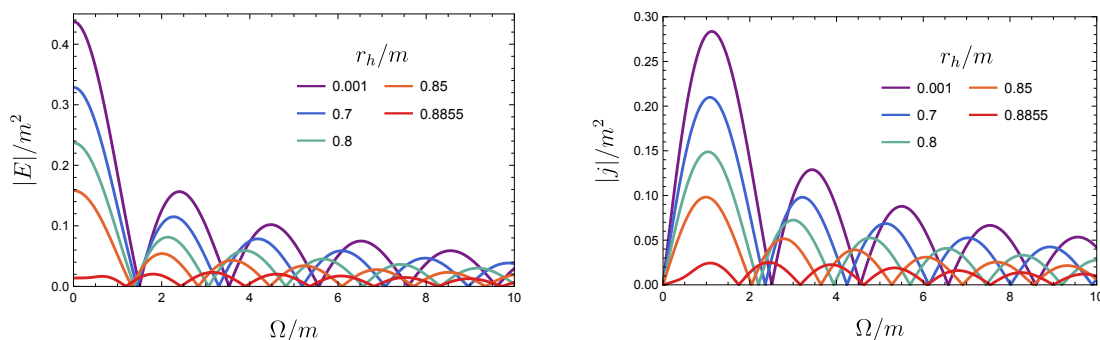


Figure 3. Electric field and current of the critical embeddings versus driving frequency, for different values of r_h in D3/D5. The frequencies for which $|E|$ vanishes are the critical frequencies Ω_c of the vector meson Floquet condensates. The regions of black hole embeddings between lobes, above such critical points, are termed *wedges* in the text. In the right plot we show the value of the current along the curve of critical embeddings. We observe points with $|j| = 0$ somewhere close to the maxima of the lobes in the left plot. We will term these points *Floquet suppression points*, and will study them in detail in section 3.1.

pause to describe the origin of this damping effect. We choose to measure dimensionful quantities in units of the quark mass. In particular, the curves above are drawn each one for a fixed value of r_h/m . Remember that both the electric field and the temperature tend to bend the probe brane towards the origin in the IR. Let us fix a mass $m = 1$ for concreteness. Then, for a small value of r_h we can still switch on and fine tune the electric field to make the embedding bend enough so as to touch the critical surface. As r_h grows, this supplemental field needed becomes less and less, which accounts for the drop in the lobe structure to be seen on the plots in figure 3. Finally, there is a maximum value for $r_h/m = 0.8897$ beyond which all the embeddings are of black hole type for any value of $|E|$ and Ω .

Figure 4 unfolds the fine structure in the vicinity of the vector meson Floquet condensates. The left (right) plots show the values of the current $|j|/m^2$ (the condensate \mathcal{C}) as a function of the applied electric field $|E|/m^2$ for different values of the rotating speed Ω . From top to bottom, the temperature increases parametrized by $r_h/m = \sqrt{2}u_h/m$. The upper case, with $r_h/m = 0.5$ is almost indistinguishable from the case with $r_h/m = 0 = T$ studied in [1, 10]. Points on the continuous (dashed) lines are for black hole (Minkowski) embeddings. From the lower left corner all curves start at the Minkowski solution with $|j| = |E| = 0$ (no singular shell). For a small value of Ω the behaviour is as shown in the blue curves with $\Omega = 1.2$. As the electric field increases a non-dissipative polarization current builds up along the dashed portion of the blue curves. At some point the curve becomes multivalued, the prelude of a presumably discontinuous phase transition to a black hole configuration (a point on the continuous curve segment upwards) where a dissipative conduction current is allowed. The nature and exact occurrence of this transition is beyond the reach of equilibrium thermodynamics where free energy evaluation is enough.

Rising the frequency Ω all the curves get displaced towards their left and, at some value Ω_c , that depends on r_h/m , contacts the axis $|E| = 0$ at a nonzero value for both $|j| > 0$ (and

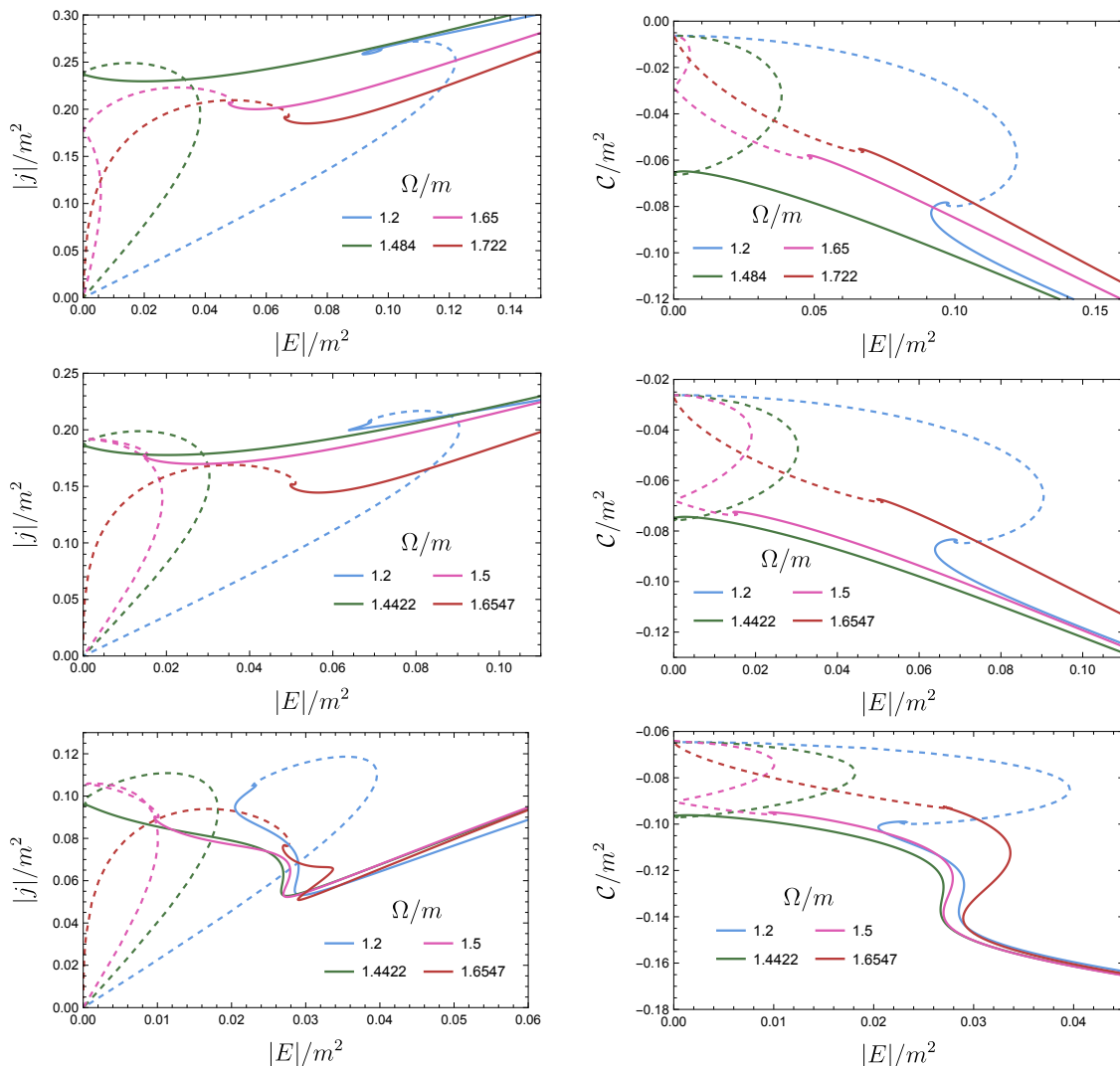


Figure 4. The dashed curves represent the insulator (Minkowski) phase and the solid curves the conductive (BH) phase (beware the opposite code with respect to [1]). Electric current $|j|/m^2$ and condensate \mathcal{C}/m^2 versus electric field for $r_h/m = 0.5, 0.7$ and 0.84 , from top to bottom. The driving frequency is fixed to some $\Omega/m < \Omega_c/m$ (blue), $\Omega/m = \Omega_c/m$ (green), $\Omega_c/m < \Omega/m < \Omega_m/m$ (pink) and $\Omega/m = \Omega_m/m$ (red). We show that E can only vanish for $j \neq 0$ for Minkowski embeddings with $\Omega_c \leq \Omega \leq \Omega_{meson}$.

also $\mathcal{C} \neq 0$) (green curves). Precise computation reveals the contact point to correspond to a critical embedding. Further increase in Ω makes this contact point slide down the vertical axis, now inside the Minkowski branch. Eventually, it reaches zero, merging again with the trivial Minkowski embedding with $|E| = |j| = 0$. All the embeddings having $|j| \neq 0$ with $|E| = 0$ build the manifold of *vector meson Floquet condensates* [10].

When r_h/m reaches 0.84 we start seeing an interference between the two horizons as they come close together. The effect is a multivaluedness in the curve of black hole embeddings that precludes the monotonic growth of $|j|$ and \mathcal{C} with $|E|$ that is seen at

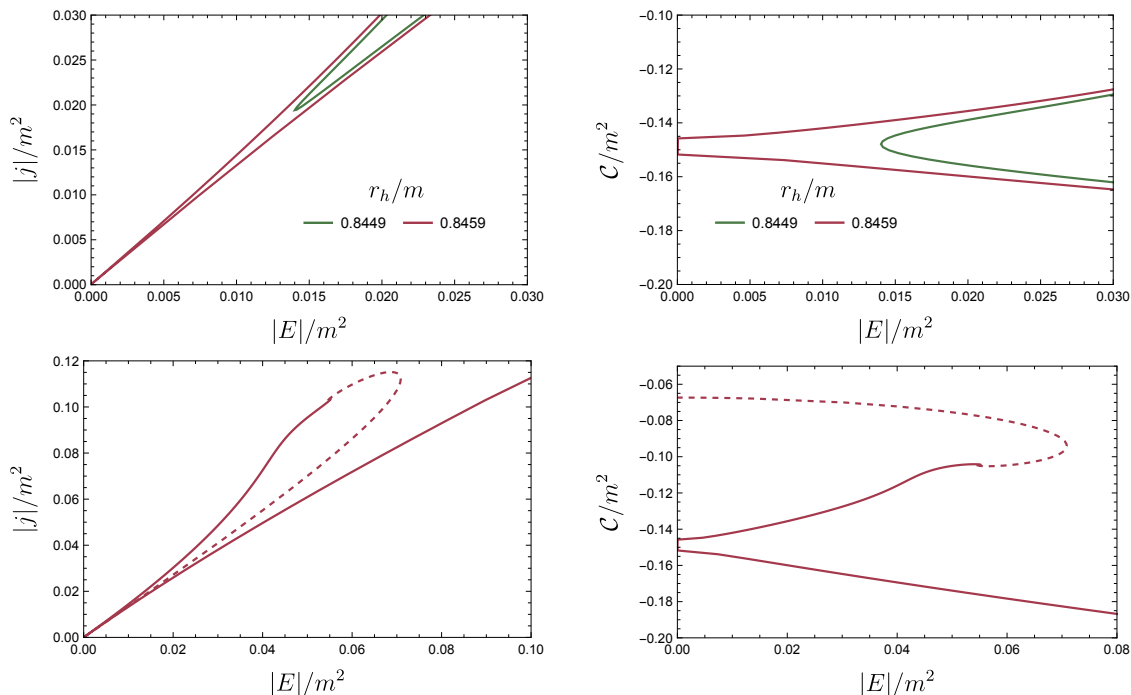


Figure 5. Electric current and condensate versus electric field for $\Omega/m = 1$. The continuous lines represent BH embeddings, while the dashed ones are the Minkowski embeddings. The upper plots show that for r_h/m around 0.845, we start getting $E/m^2 = 0$ for BH embeddings. The lower plots are the full curves for the $r_h/m = 0.8459$ case. Notice that the electric field increases again, to recover the limit $|j| = \sigma|E|$.

lower temperatures. In all cases, in the large field regime, the Ohmic behaviour $|j| = \sigma|E|$ with constant σ is reached. However, in the small interval $r_h/m \in (0.84, 0.8897)$, this regime is not approached monotonically, and we find a multivaluedness of $|j|$ and C as functions of $|E|$. This looks similar to the multivaluedness encountered in [20] within the superconducting phase. We, however, encounter this multivaluedness in the conducting phase (the normal phase there). In figure 5, we see the interference effect between the two nearby horizons is so effective that a trivial configuration with $|j| = |E| = 0$ is again attained, but now inside the branch of black hole embeddings.

In figure 6 we have promoted the list of frequencies in each of the plots in figure 4 to a third Ω axis, where the associated curves are sections of a 3D surface. On the bottom plane $|E| = 0$ the surfaces intersect in a curve which is the full manifold of vector meson Floquet condensates. The curve interpolates between two endpoints. On one end, $|j| = 0$, and we find the frequencies corresponding exactly to the vector meson masses i.e. the fluctuations in the probe brane worldvolume gauge field [21]. We have checked this in appendix F (see figure 13 for the first three meson masses). The other end, with $|j| > 0$, corresponds to a critical embedding. Turning on r_h causes an overall shift of this curve towards lower values of Ω , which can be inferred from the movement of the extreme points as shown on the lower right plot in figure 6.

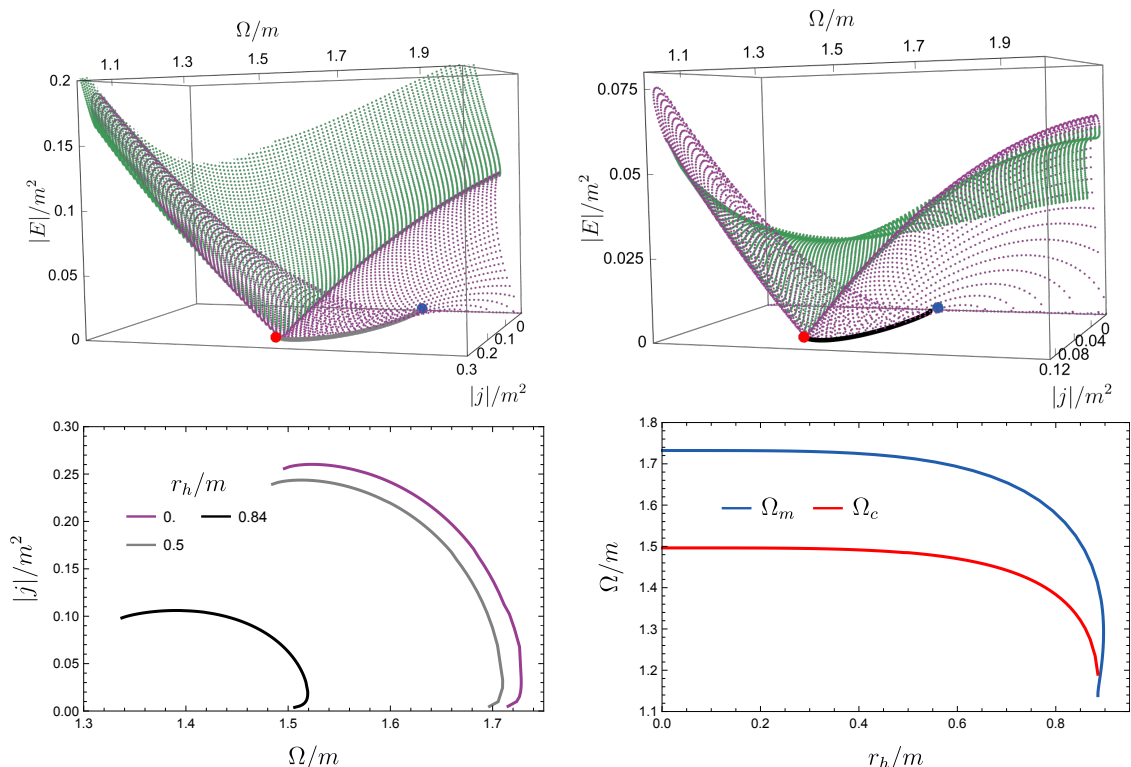


Figure 6. *Top:* 3D development of the lobed curves in figure 3 in the vicinity of the first critical point, with an extra Ω axis, for $r_h/m = 0.5$ (left) and $r_h/m = 0.84$ (right). Magenta (green) surfaces belong to the Minkowski (BH) phase. Beware the difference in vertical scales. The purple or blue dots are Minkowski embeddings and the green or red ones BH embeddings. The gray thick lines represent the $|E| = 0$ vector meson Floquet condensates. *Lower left:* vertical view of the upper left plot where the gray lines in the upper left plot have been graphed for three different temperatures. *Lower right:* movement of the two extreme points in the curve as a function of r_h . They are the critical embedding and the first meson mass frequency respectively. We see that the effect of the background temperature is mild (less than 10%) until the value $r_h/m \sim 0.8$ is reached.

On general grounds, the influence of the temperature on the results at $r_h = 0$ is small until we approach the maximum temperature $r_h/m = 0.8897$, hence, when the lobes in figures 3 are very small. Regarding the upper plots in figure 6, observe how the manifold of black hole embeddings folds down for the right plot $r_h/m = 0.85$ in contrast with the monotonic growth on the left one, at $r_h/m = 0.5$. This is precisely the multivaluedness remarked for higher temperatures inside the branch of BH embeddings.

To finish this section, let us comment on the possibility of accurately locating the first order phase transitions where the phase space curves become multivalued. The usual prescription of comparing the free energies is valid in thermodynamical equilibrium. The usual holographic prescription that proposes the euclidean gravitational action for such a construct is not working properly in the present context of a non-equilibrium steady state (see [20] for similar concerns and [22] for a review on the topic). A more sophisticated

approach using techniques tailored for non equilibrium open systems as applied to the holographic context is an interesting project to carry out also here. Eventually, an exact dynamical simulation with a slowly varying $|E|/m^2$ should be the right thing to do.

3.1 Floquet suppression points

In figure 3, on the right plot, we already mentioned the presence of points within the line of critical embeddings where the current vanishes $|j| = 0$ even in the presence of nonzero electric field. They roughly coincide with the points where the electric field becomes maximal within the same family. We will term these points *Floquet suppression points* and the corresponding states *Floquet-suppressed states*. As we will show, the existence of these points extends to the Minkowski embeddings and, in a sense to be explained in the next section, also to the black hole embeddings. Focusing on critical and Minkowski embeddings, we have already mentioned that the current has its origin in the polarizability, $\tilde{\pi}$, of the vacuum, $\mathcal{P} = \tilde{\pi}\mathcal{E}$, with $\mathcal{P} = \langle \bar{\psi}(\gamma_x + i\gamma_y)\psi \rangle$ [10]. Hence $\mathcal{J} = \dot{\mathcal{P}} = i\Omega\tilde{\pi}\mathcal{E}$ and a vanishing value of $\mathcal{J} = 0$ implies $\tilde{\pi} = 0$, i.e. the polarizability is *dynamically* suppressed.

This suppression of the vacuum polarizability for certain frequencies is similar to well known (and searched for) dynamical effects in other examples of Floquet engineering. For example, in periodically driven lattices, hopping between neighbouring sites, although present in the bare hamiltonian, can be completely suppressed by tuning the ratio of frequency to amplitude, leading to induced dynamical localization (see [2, 6, 7] for references).

Figure 4 is built by scanning frequencies $\Omega \in (1.2, 1.7)$, i.e., around the point of the first vector meson Floquet condensate. In figure 7 we show, on the upper left plot, the similar curves setting instead $\Omega \in (2.3, 2.7)$, that is, in a small interval around the first Floquet suppression point. The result exhibits a remarkable similarity, but with $|j|/m^2$ and $|E|/m^2$ axes exchanged. Indeed the symmetry is not exact, as can be seen by comparing the curves in the lower left plots in figures 6 and 7. These are respectively the curves of vector meson Floquet condensates and Floquet suppression points. End points on the lower axis can be obtained in both cases by studying the linearized fluctuations of the world-volume gauge field subject to the boundary conditions $|E| = 0$ and $|j| = 0$ respectively. At zero temperature this calculation can be performed analytically giving (see [1] eqs. (C.2) and (C.3))

$$|E| = 0 \rightarrow \Omega_n = 2\sqrt{\left(n + \frac{1}{2}\right)\left(n + \frac{2}{2}\right)} = 1.732, 3.873, \dots$$

$$|j| = 0 \rightarrow \Omega_k = 2\sqrt{k(k+1)} = 2.828, 4.899, \dots$$

Upon rising the temperature, $r_h > 0$, these quantities get shifted downwards, as shown on the lower right plots in figures 6 and 7. The (almost) symmetry between vector meson Floquet condensates and Floquet suppression points is highlighted on the top right plot of figure 7, where both manifolds have been included within the same 3D development.

It is worth mentioning that the existence of these Floquet suppression points is not restricted to the D3/D5 system, hence is not apparently linked to the dimensionality. For completeness we devote appendix G to the twin version of this section in the context of a D3/D7 scenario. Apart from the discrepancy in the precise numerical values, the global

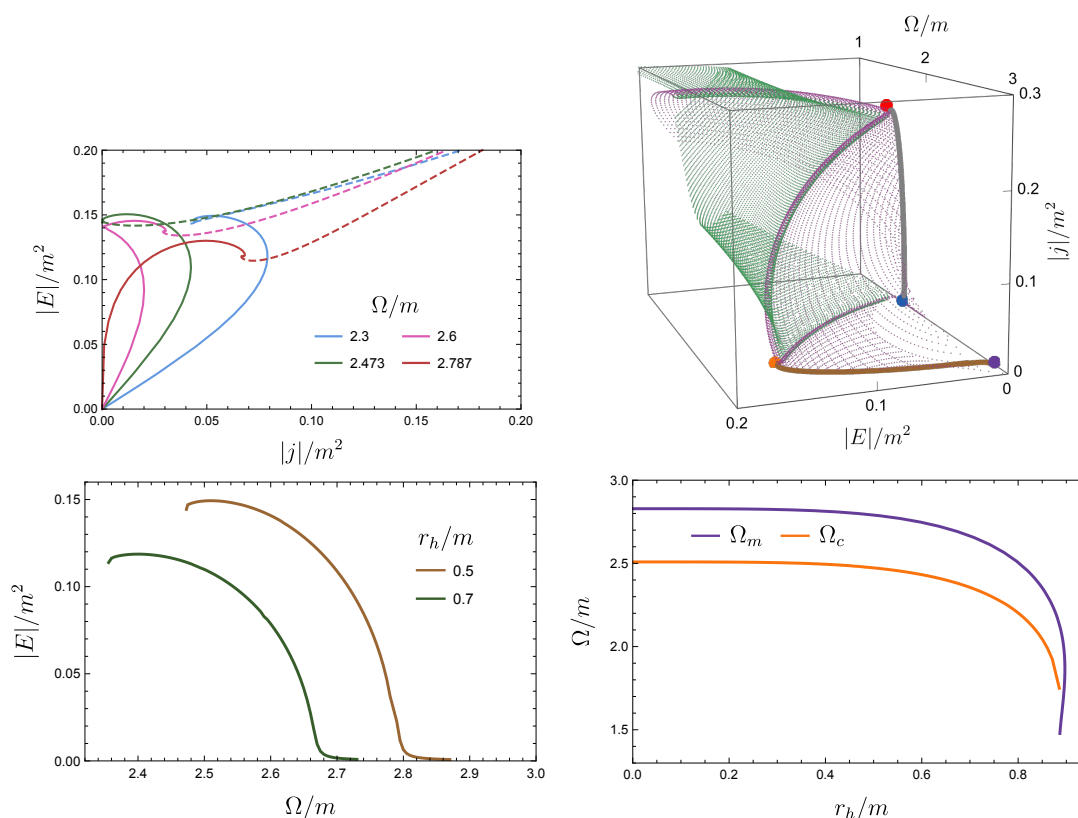


Figure 7. *Top:* on the left, plots of $|j|/m^2$ vs. $|E|/m^2$ where we exchanged the axes to make apparent the striking similarity with the plots in figure 4. On the right, 3D plot where the range of Ω has been extended to cover the first vector meson Floquet condensate (grey curve at $|E| = 0$) as well as the first Floquet suppressed condensate (brown curve at $|j| = 0$). *Bottom:* the left plot shows view of the $|j| = 0$ plane of the upper plots. The suppressing effect of the temperature is apparent. The right plot is the downshift in Ω of the two extreme points (orange and violet) in the plot above this, as a function of r_h/m .

picture is the same. For example, in figure 14 we reproduce the lobe structure for the D3/D7 system, which is analogous to the one found in figure 3 for D3/D5. Also the $(|j|/m^2, |E|/m^2)$ curves in figure 15 are very similar counterparts of the ones in figures 4 and 7.

4 Non-linear conductivity

The relation between the current vector and the electric field vector defines a *rotating current (RC) conductivity*²

$$j = \tilde{\sigma}_{RC} E \tag{4.1}$$

²Notice that in the rotating frame we write $\tilde{\sigma}_{RC}$ as we are dealing here with a single Fourier component Ω of the rotational time dependence. In general, in the lab frame, we would write instead $\mathcal{J}(t) = \int d\tau \sigma_{RC}(\tau) \mathcal{E}(t - \tau)$. Also the use of complex instead of vector notation is implicit.

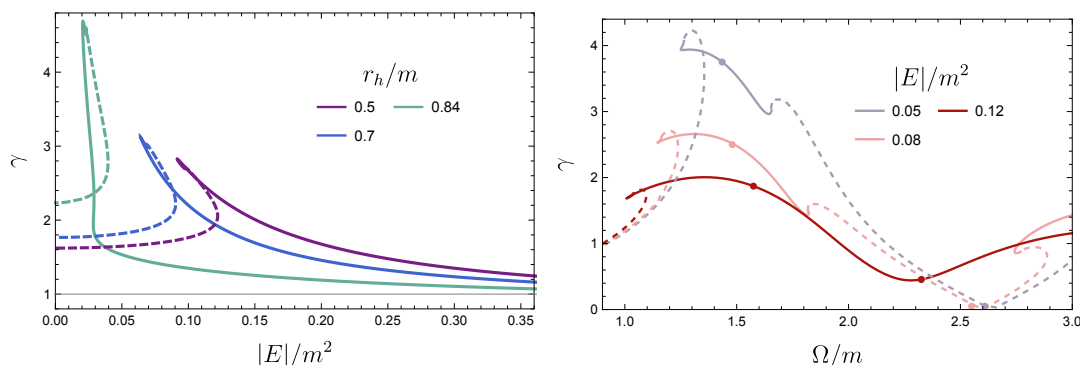


Figure 8. Modulus of the non-linear conductivity $\gamma = |\tilde{\sigma}_{RC}|$ as a function of $|E|/m^2$ for fixed $\Omega/m = 1.2$ (left plot) or as a function of Ω/m for fixed values of $|E|/m^2$ (right plot). For large $|E|/m^2$ the curves asymptote to the value $\gamma = 1$.

where $\tilde{\sigma}_{RC}(\Omega, |E|)$ is a complex number which is, itself, a non-linear function of $|E|$ (by rotational symmetry) and Ω . Writing

$$\tilde{\sigma}_{RC} = \gamma e^{i\delta}$$

the modulus γ is the non-linear conductivity whose value is plotted in figure 8. The phase δ encodes the angle between the instantaneous vectors $\vec{j} = (j_x, j_y)$ and $\vec{E} = (E_x, E_y)$. This is why we will refer to δ as the angle, even if we use complex instead of vector notation. For a given $|E|$ this relative angle controls the Joule heating (2.17)

$$q = \gamma |E|^2 \cos \delta.$$

Its microscopic origin is unclear although we will make an attempt to put forward a consistent picture after we have collected all the bits and pieces.

For Minkowski embeddings \vec{j} and \vec{E} are perpendicular and $q = 0$. This is consistent with the picture of the polarization of the meson condensate into dipoles aligned with the electric field. It leaves two possibilities for $\delta = \pm\pi/2$. In ref. [10] only the positive sign was considered, as it is natural to think that the polarization and the electric field are parallel vectors. We will show here that the existence of both signs is a natural consequence of the presence of Floquet suppression points.

In figure 9 we observe the behaviour of the relative angle δ as we scan embeddings along the horizontal lines of constant $|E|$ while increasing Ω , as shown in the right plot. As usual, BH (Minkowski) embeddings belong to solid (dashed) segments. On the left plot, using the same color coding, we can see the value of the angle, δ , as we move along these sets of solutions. Notice the jumps $\delta = \pi/2 \rightarrow -\pi/2$ that occur within the dashed segment, i.e. for Minkowski embeddings. They seem to reflect a discontinuous transition but this is not the case. Indeed, looking at the right plot in figure 8 we see that, precisely at those points, we find a vanishing value for the module of the polarization current $\gamma = 0 \Rightarrow |j| = 0$. The corresponding Ω frequencies have been signalled with a dot on the right plot in figure 9. Joining all such Floquet suppression points yields the green dashed curve which is, precisely, the same curve represented in the lower left plot of figure 7, also in (solid) green.

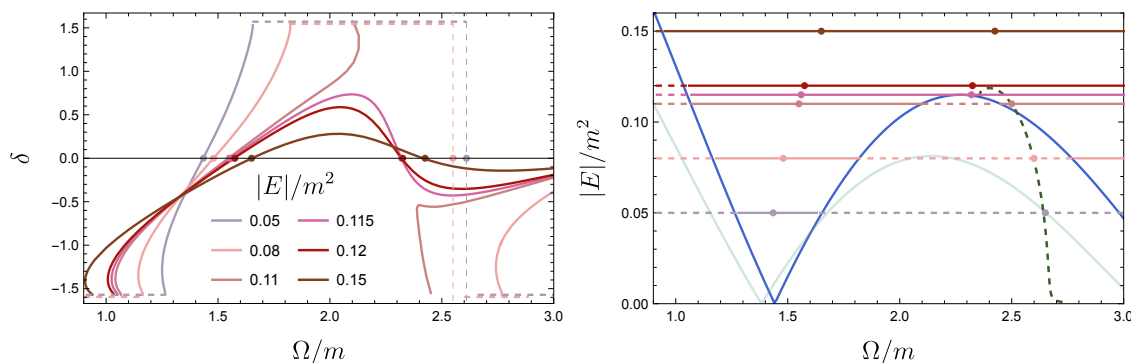


Figure 9. Continuous lines are black hole embeddings, whereas dashed lines are Minkowski (with a slight vertical offset for clarity). *Left:* relative angle δ for different embeddings at various fixed values of the electric field and with $r_h/m = 0.7$ for varying Ω/m . *Right:* this is a zoom of the first lobe region in figure 3, where the color code for constant $|E|/m^2$ lines corresponds to the ones on the left plot. The dots indicate the frequencies where the angle δ either becomes zero in the BH segments, or flips sign in the Minkowski segments. In this later case, joining all the points gives the dashed green curve. The fact that this curve of Minkowski embeddings exits the lower lobe is related to the spiralling multivaluedness of the phase space curves in the vicinity of the critical embeddings. We have added another (dimmed green) lobed curve with higher temperature $r_h/m = 0.8$ to show that the effect of rising the temperature is similar to that produced by increasing the electric field $|E|/m^2$.

In summary, the transition $\delta = \pi/2 \rightarrow -\pi/2$ occurs through a Floquet-suppressed state where the polarizability $\tilde{\pi}$ vanishes and transits smoothly from positive to negative. This is remarkable as it states that, for ample intervals in the range of driving frequencies Ω , the meson condensate is polarized *antiparallel* to the applied electric field!

Looking back to the left plot in figure 9 we notice that the opposite transition $\delta = -\pi/2 \rightarrow +\pi/2$ is *not* discontinuous. It occurs through a sequence of black hole embeddings that interpolate between those values along a curve that crosses smoothly the axis $\delta = 0$ with finite slope. A look at the right plot in figure 8 reveals that, in contrast, at those points γ stays strictly positive.

Putting all the information together the interpretation we find most plausible is as follows: in general, the total current will be an admixture $j = j_{\text{con}} + j_{\text{pol}}$ of conduction (dissipative) and a polarization (conservative) currents [23, 24]. The precise contribution of each component is controlled by the driving frequency Ω and by $|E|$. The conduction component j_{con} , embodied by deconfined charged carriers, is parallel to the applied electric field. The polarization component j_{pol} , as explained above, is perpendicular. The vector sum of these two components gives j and E a relative phase angle δ .

Changing Ω at fixed $|E|/m^2$, like on the left plot in figure 9, we find that j_{pol} vanishes at given frequencies Ω , thereby flipping $\delta = \pm\pi/2 \rightarrow \mp\pi/2$. In the gapped (Minkowski phase) only this component of the current is present. In the gapless (BH) phase, both components generically contribute. We interpret the points where $\delta = 0$ as precisely signalling that, there also, $j_{\text{pol}} = 0$. Thereby the total current becomes parallel to the electric field. This is the reason why the transition in δ is continuous in the BH phase

(solid segments). If this picture makes sense, the conclusion is that *we also have Floquet suppression points within the BH phase*. It is just that in the BH phase this vanishing is masked by the conduction component $j = j_{\text{con}} + 0$. In summary, all the dots in figure 8 and 9 correspond to Floquet suppressed states. As we approach the boundaries of these segments, the conduction component disappears $j_{\text{con}} \rightarrow 0$, and the polarization component survives making $j = j_{\text{pol}}$ and E mutually perpendicular again.

For large enough $|E|/m^2$ we always stay within the phase of BH embeddings, and the (solid) curves smoothly relax down to the asymptotic regime where $\delta = 0$. We interpret this as the vanishing of the j_{pol} component in this limit. This is the same effect we get for large temperature $T/m \gg 1$ as both are indistinguishable from the limit of small mass $m \rightarrow 0$.

In appendix D.1 we prove exactly this fact, $\tilde{\sigma}_{RC} = 1$, for massless flavors. This implies that, in this case, the response is both instantaneous and linear. We make contact and fully agree here with the results in [12]. In a sense, the claim there is stronger as it applies to *any* time dependence of a linearly polarized electric field $\mathcal{E}_x(t)$ at the boundary. Here, on one side, we go to a rotational polarization ansatz and, moreover, in appendix D.2 we prove this result to hold also at linearized order in a small mass δm . Linearity of the response entails that it should also extend to arbitrary two dimensional time dependent electric fields $\vec{\mathcal{E}}(t)$ at linear order in small masses.

5 Photovoltaic optical conductivity

The Floquet engineering of an induced Hall effect is termed usually photovoltaic Hall effect [25]. In [9], following the proposal in [26], the photovoltaic optical response was obtained for massless charge carriers in the D3/D7 model and an optical Hall current was found. We extended this study in [1] to massive flavors in the D3/D5 model, and observed an intricate behaviour in the wedge region between the lobes in figure 3, with multiple resonance peaks present. The physics in this wedge is presumably controlled by the vector meson Floquet condensate at zero temperature, that signals the presence of a quantum phase transition. In the present work, first, we would like to see how the presence of a temperature affects those results.

The results are contained in the plots shown in figure 10. The curves represent the absorption spectrum $\sigma_{xx}(\omega)$ and the Hall conductivity $\sigma_{xy}(\omega)$. The background rotating electric field has been fixed to $|E|/m^2 = 0.1$. Its frequency has been set to the first critical frequency $\Omega_c(r_h)$ which decreases with the temperature as seen in the lower right plot of figure 6. The band in which these values lie for the chosen temperatures has been signalled by a vertical band in pink. The curves for σ_{xx} and σ_{xy} show a smooth deformation of the ones in [1] (figure 10) for the same value of $|E|/m^2$.

Succinctly stated, the temperature in the gluon bath, in general destroys the AC Hall optical conductivity, and hence, also the DC Hall conductivity. Again, the effect of the temperature is similar to the one caused by the increase in electric field. Namely, the conductivity peaks get roughened and lowered. In a sense, both agents, the temperature and the electric field act in parallel by enhancing the amount of deconfined charge carriers in the medium.

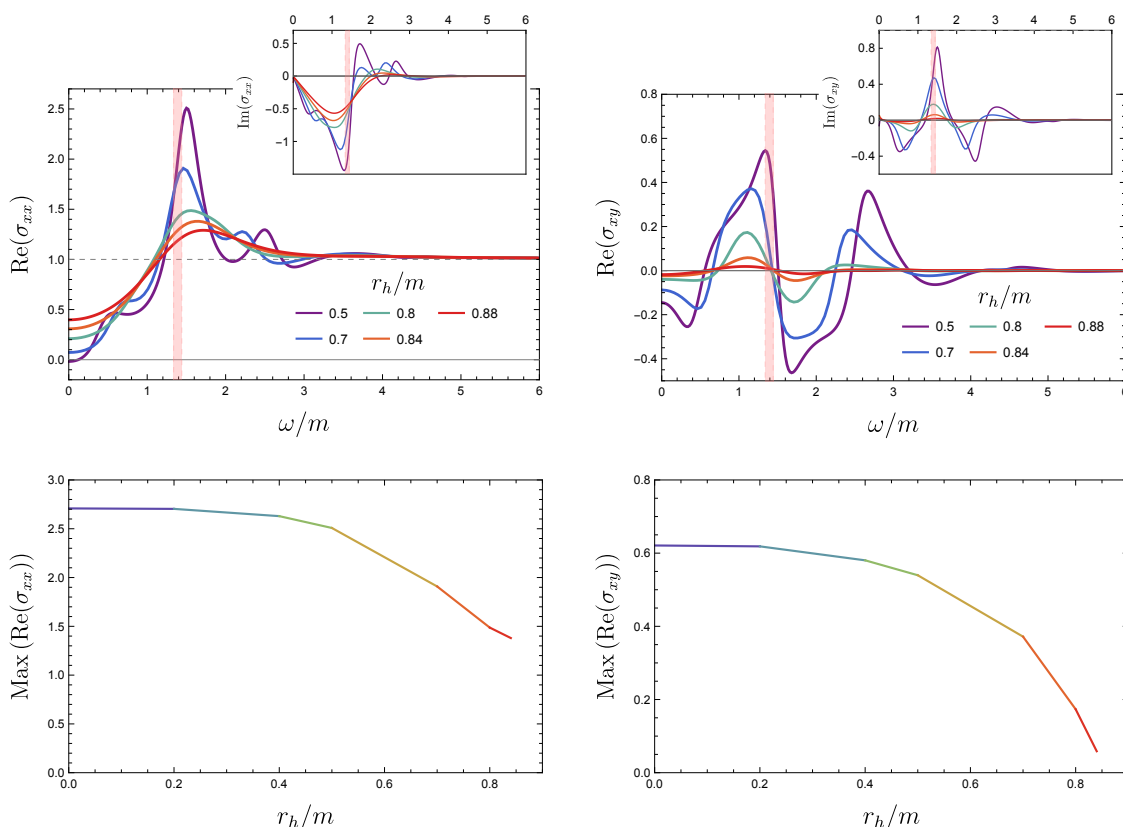


Figure 10. *Top:* AC conductivities for four values of r_h at their corresponding $\Omega_c(r_h)$, for $E/m^2 = 0.1$. The pink band marks the range where the four values of $\Omega_c(r_h)$ belong. The main peak is close to this region. *Bottom:* variation with the temperature of the maximum value of the real part of σ_{xx} and σ_{xy} for $E/m^2 = 0.1$

The effect becomes more pronounced beyond some temperature $r_h/m \sim 0.5$, as shown in the lower plots of figure 10. In the large temperature limit, $r_h \rightarrow \infty$, all conductivities, both AC and DC tend towards $\sigma_{xx} = 1$, $\sigma_{xy} = 0$ (see figure 11). This result is the same we obtained for the rotating current conductivity $\tilde{\sigma}_{RC}$ in the massless limit. Since in this case the electric field is linearly polarized, rather than circularly, we see this as a further evidence in favor of the fact that the response will be Ohmic and instantaneous for an arbitrary time dependence of the electric field in the plane $j(t) = \sigma E(t)$.

A peculiar observation is that the frequencies ω of highest peaks in the absorption spectrum $\text{Re}(\sigma_{xx})$ slightly deviate above the one of the driving $\omega \gtrsim \Omega$ (within the vertical band in pink). This was also observed in [1] (figure 10) where the drift is seen to be enhanced with increasing $|E|$. We could not offer any explanation to this. Here we can see that there is a very similar shift in the driving frequencies Ω of the Floquet suppression points inside the BH phase (solid segments) in figure 9 with increasing $|E|$ towards the right. We have tried to make sense of this qualitative coincidence but could not find an exact numerical agreement.

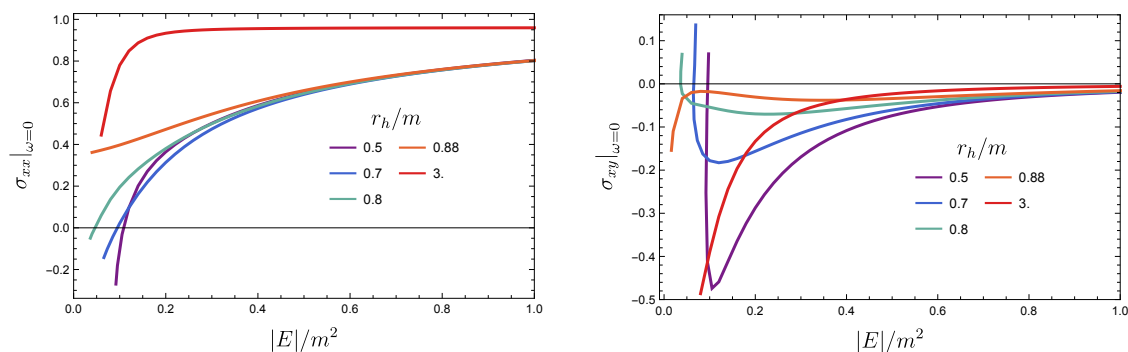


Figure 11. DC conductivities as functions of $|E|/m^2$ for different values of r_h/m at $\Omega/m = 1$. At high temperatures the conductivity tensor tends towards the identity $\sigma_{xx} = 1$ and $\sigma_{xy} = 0$.

6 Summary and outlook

This paper pursues, along the line of previous works [1, 10], the study of holographic Floquet flavour systems driven by an external rotating electric field. We focus on the D3/D5 system but we find that most of the results are qualitatively robust and shared by the D3/D7 setup. We have sharpened our findings in [1] in several directions.

First, we studied the effects of having the system heated at some non-zero temperature. In this case, the dual geometry has two types of horizons: the usual event horizon of the closed string geometry in the bulk, and the effective horizon of the open string metric on the brane. Respectively, we can associate two temperatures to them: the Hawking temperature T of the background (see (2.3)) and the effective one T_{eff} written in (2.12) experienced by the worldsheet degrees of freedom. We have scanned throughout all our phase space and checked that $T_{\text{eff}} > T$.

The main effect of the background temperature is the addition of deconfined charged carriers to the system. Such carriers add to the ones produced by the electric field through the Schwinger mechanism of dielectric breakdown. We show that one of the main results in previous works, namely, the presence of vector meson Floquet condensates, persists at finite temperature, signalling the robustness of this non-perturbative effect. The lobbed structure of the line of critical embeddings is also found here, but gets depleted in height and is completely washed away for high enough values of the temperature, namely, for a radius horizon $r_h/m \geq 0.8897$ in units of the quark mass (see figure 3).

At high temperatures, some interesting effects occur when the background and effective horizons come close together. These include a multi-valuedness that resemble a secondary phase transition within the conductive black hole phase (figure 4). Also new solutions with vanishing $|E| = |j| = 0$ appear within this phase (figure 5).

Secondly, we have remarked the relevance of the so called *Floquet suppression points*. These states were missed in previous analysis but are common to both D3/D5 and D3/D7 systems both at zero and finite temperature. We have shown that the phase portrait very close to these points is strikingly similar to the one in the vicinity of the vector meson Floquet condensates, up to an exchange of j with E . This calls for a deeper study in

search for a sounder duality. From the physical point of view, these new points exhibit a dynamical suppression of the vacuum polarizability. It could be attributed to a dynamical screening of the effective dipole charge of the meson fluctuations at strong coupling and for precise frequencies. It bears resemblance to similar effects in the realm of Floquet condensed matter systems where, for example, hopping terms can be seen to vanish at finely tuned frequencies of the driving. This is the type of effects that make Floquet driving an appealing paradigm in the search for mechanisms that could help in suppressing quantum decoherence.

Thirdly, we have also pursued the analysis initiated in [1] concerning the non-linear rotating conductivity in section 4. The relative phase (angle) between j and E has an interesting information that we interpret in terms of a possible variable admixture of two types of currents: rotating polarization and charge flow. The polarization current is the only one present in the Minkowski phase while both are present in the BH states. The global picture that emerges from the analysis, shows that the Floquet suppressed states are points where the polarizability of the vacuum switches smoothly from positive to negative. This is remarkable as it states that, for ample intervals in the range of driving frequencies, Ω , the meson condensate is polarized *antiparallel* to the applied electric field! Again here, this result is amongst the class of remarkable effects that one can find in the context of Floquet engineering [7] of condensed matter systems. For example, it is worth citing ref. [27], where paramagnetism can be turned into diamagnetism under a strong driving in the Rabi model coupled to a heat bath.

In the limit of large electric field, and/or large temperature, we agree with the results in [12]. In this limit the polarization rotating current gets suppressed, $j_{\text{pol}}(t) \rightarrow 0$, whereas the conduction current satisfies an Ohmic instantaneous response for an arbitrary frequency of the rotating driving $j(t) \sim j_{\text{con}}(t) = \sigma E(t)$ with σ a real constant. Linearity suggests the possibility of this being also true for any electric field time dependence in 2+1 dimensions.

Last but not least, we have examined the optical AC and DC conductivities in the presence of a driving. The interesting pattern with peaks found in [1] deep inside the wedges between the lobes in phase space still exists for low to moderate temperatures, but gets dissolved as soon as the height of the lobes is depleted at high temperature. The highest peaks shift with growing $|E|$ and stay close to the position of the (also drifting) Floquet suppression points. However we haven't found exact numerical agreement, so this stays a qualitative observation. We also find agreement with the predictions in [12] in the limit of small mass.

Our work could be continued along several directions. One clear option would be to add chemical potential and/or magnetic components to the gauge field in order to explore the complete phase space of the D3-D5 model. To verify the universality of our results we could consider the ABJM model [28] driven by a rotating electric field. This last model has a rich topological structure and is dual to a $(2+1)$ -dimensional conformal field theory. The flavor branes in this case are D6-branes [29, 30] (the thermodynamics of these flavor branes has been studied in [31]). Another direction worth pursuing is the analysis of the effects of backreaction for a large number of flavor branes. Interestingly, backreacted D3-D5 backgrounds have been constructed in [32–35] using the smearing approximation reviewed

in [36]. One could also study the driving generated by moving the brane periodically in time (i.e. oscillating or rotating). This type of configurations were considered in [37, 38], and are the natural setup to find resonances that could be interpreted as Floquet condensates of other type of mesons, like scalar mesons.

Finally, another aspect that deserves further attention is the actual nature of the phase transition. It can be triggered by an admixture of both temperature and/or electric field. While the multi-valuedness of the state curves in figure 4 suggest an area law for the transition point, the actual location it is not consistent for the $(|j|/m^2, |E|/m^2)$ and the $(\mathcal{C}, |E|/m^2)$ curves. This points to the difficulties, out of equilibrium, in defining a *bona fide* free energy from which the 1-point functions are derived [20]. Techniques developed specifically for open non equilibrium steady states should be used instead. In particular, it would be very interesting to apply the Schwinger-Keldysh approach of [39, 40] to these systems in order to calculate properties of the corresponding steady states like equilibrium of phases and phase transitions.

Acknowledgments

We are indebted for valuable mail exchanges with Takaaki Ishii, Arnab Kundu, Carlos Hoyos, Keiju Murata, Andy O’Bannon, Kostas Skenderis and Julian Sonner.

This work has received financial support from Xunta de Galicia (Centro singular de investigación de Galicia accreditation 2019-2022 and grant ED431C-2021/14), by European Union ERDF, and by the “María de Maeztu” Units of Excellence program MDM-2016-0692 and the Spanish Research State Agency (grant PID2020-114157GB-100).

A Coordinates and D5-brane action

The ten-dimensional black hole metric generated by a stack of D3-branes is:

$$ds_{10}^2 = \left(\frac{r}{R}\right)^2 \left(-f(r) dt^2 + dx_3^2\right) + \left(\frac{R}{r}\right)^2 \left(\frac{dr^2}{f(r)} + r^2 d\Omega_5^2\right), \quad (\text{A.1})$$

where R is the anti-de Sitter radius, $d\Omega_5^2$ is the line element of a unit five-sphere and $f(r)$ is a blackening function given by:

$$f(r) = 1 - \left(\frac{r_h}{r}\right)^4, \quad (\text{A.2})$$

where the horizon radius r_h is related to the black hole temperature as:

$$T = \frac{r_h}{\pi R^2}. \quad (\text{A.3})$$

Let us now rewrite the line element (A.1) in a coordinate system more convenient for our purposes. First of all, we split $d\Omega_5^2$ as:

$$d\Omega_5^2 = d\theta^2 + \cos^2 \theta d\Omega_2^2 + \sin^2 \theta d\hat{\Omega}_2^2, \quad (\text{A.4})$$

where $d\Omega_2^2$ and $d\hat{\Omega}_2^2$ are line elements of two two-spheres. Moreover, let us introduce the so-called *isotropic coordinate* u :

$$u^2 = \frac{r^2}{2} \left(1 + \sqrt{1 - \frac{r_h^4}{r^4}} \right), \quad (\text{A.5})$$

with the horizon sitting at $u_h = r_h/\sqrt{2}$. We also define

$$\psi = \sin \theta. \quad (\text{A.6})$$

Then, the metric (A.1) becomes:

$$ds_{10}^2 = \frac{u^2}{R^2} \left(-\frac{g(u)^2}{h(u)} dt^2 + h(u) dx_3^2 \right) + \frac{R^2}{u^2} du^2 + R^2 \left(\frac{d\psi^2}{1-\psi^2} + (1-\psi^2) d\Omega_2^2 + \psi^2 d\hat{\Omega}_2^2 \right), \quad (\text{A.7})$$

where $g(u)$ and $h(u)$ are the functions:

$$g(u) = 1 - \frac{u_h^4}{u^4}, \quad h(u) = 1 + \frac{u_h^4}{u^4}. \quad (\text{A.8})$$

The action of the probe brane is given by the DBI action

$$I_{D5} = -N_f T_5 \int d^6 \xi \sqrt{-\det (g_6 + 2\pi \alpha' \mathcal{F})}, \quad (\text{A.9})$$

where T_5 is the tension of the D5-brane, g_6 is the six-dimensional induced metric on the worldvolume of the D5-brane and $\mathcal{F} = d\mathcal{A}$ is the worldvolume gauge field strength.

Let us embed the D5-brane in such a way that one of the cartesian coordinates is constant and the brane sits at fixed point of the second two-sphere with $\psi = \psi(u)$. Then, the induced metric becomes:

$$ds_6^2 = \frac{u^2}{R^2} \left(-\frac{g^2(u)}{h(u)} dt^2 + h(u) dx_2^2 \right) + R^2 \left(\frac{1}{u^2} + \frac{\psi'^2}{1-\psi^2} \right) du^2 + R^2 (1-\psi^2) d\Omega_2^2. \quad (\text{A.10})$$

Let us write down explicitly the action of the probe D5-brane. For simplicity in what follows we will take $R = 1$. When $\mathcal{F} = d\mathcal{A}$ and the one-form \mathcal{A} is given by the ansatz (2.6), the DBI action can be written as:

$$\frac{I_{D5}}{\mathcal{N}} = - \int du \mathcal{L}, \quad (\text{A.11})$$

where $\mathcal{N} \equiv 4\pi N_f T_{D5} \text{vol}(\mathbb{R}^{1,2})$ and the lagrangian density \mathcal{L} is given by

$$\mathcal{L} = \sqrt{(1-\psi^2) [(u^4 g^2 - \Omega^2 b^2) ((1-\psi^2) b'^2 + h(1-\psi^2 + u^2 \psi'^2)) + (1-\psi^2) u^4 g^2 b^2 \chi'^2]}. \quad (\text{A.12})$$

In (A.12) the phase $\chi(u)$ only appears through its derivative $\chi'(u)$. So a conserved quantity, q , can be defined as

$$q \equiv \Omega \frac{\partial \mathcal{L}}{\partial \chi'} = \chi' \frac{u^4 \left(1 - \frac{u_h^4}{u^4} \right)^2 \Omega b^2 (1-\psi^2)^2}{\mathcal{L}(\psi, \psi', b, b', \chi')} = \frac{(u_c^4 - u_h^4)^2}{u_c^4} (1-\psi_0^2) \quad (\text{A.13})$$

where the last equality is the one obtained by imposing reality of the Routhian action (2.10) at the singular shell. Therefore, it is a cyclic variable that can be written in terms of the other functions as

$$\chi' = \frac{q}{u^2 b g(u)} \sqrt{h(u) + b^2 + \frac{u^2 h(u) \psi'^2}{1 - \psi^2}} \frac{\sqrt{\Omega^2 b^2 - u^4 g(u)^2}}{\sqrt{q^2 - u^4 \Omega^2 b^2 g(u)^2 (1 - \psi^2)^2}}, \quad (\text{A.14})$$

where q is the constant of motion defined in (2.9). Near the UV boundary, the fields $\psi(u)$, $b(u)$, $\chi(u)$ behave as

$$\begin{aligned} \psi(u) &= \frac{m}{u} + \frac{\mathcal{C}}{u^2} + \mathcal{O}(u^{-4}), \\ b(u)e^{i\chi(u)} &= \frac{iE}{\Omega} + \frac{j}{u} + \mathcal{O}(u^{-2}). \end{aligned} \quad (\text{A.15})$$

At the singular shell, the fields $\psi(u)$, $b(u)$, $\chi(u)$ can be written as

$$\begin{aligned} \psi(u) &= \psi_0 + \psi_1(u - u_c) + \dots, \\ b(u) &= b_0 + b_1(u - u_c) + \dots, \\ \chi(u) &= \chi_0 + \chi_1(u - u_c) + \dots, \end{aligned} \quad (\text{A.16})$$

where $\psi_0 = \psi(u = u_c)$, $b_0 = b(u = u_c)$, $\chi_0 = \chi(u = u_c)$ (χ_0 can be set to 0). The coefficients χ_1 , ψ_1 and b_1 are fixed by the equations of motion, and are given by

$$\begin{aligned} \chi_1 &= \frac{\Omega}{g(u_c)u_c^3} \sqrt{\sqrt{C(1+C)} \left[2\Omega^2 C^2 + \frac{1}{2}(\Omega^2 + 4h(u_c)u_c^2) \right] - \frac{1}{2}C \left[(3+4C)\Omega^2 + 4h(u_c)u_c^2 \right]}, \\ \psi_1 &= \frac{1}{2h(u_c)u_c^2} \left(BC - \sqrt{A(1+C)} \right), \\ b_1 &= -\frac{\Omega}{u_c} \left(\frac{1}{2} + C - \sqrt{C(1+C)} \right), \end{aligned} \quad (\text{A.17})$$

where the constants A , B , C are given by

$$\begin{aligned} A &= (1 - \psi_0^2)h(u_c)[\Omega^2 + 4h(u_c)u_c^2], \\ B &= 2\psi_0 g(u_c)u_c, \\ C &= \frac{A}{B^2}. \end{aligned} \quad (\text{A.18})$$

The Minkowski embeddings close off smoothly above the horizon at some $u_0 > u_c$. At u_0 we can write

$$\begin{aligned} \psi(u) &= 1 - \frac{3(u_0^4 + u_h^4)(u_0^8 + u_h^8 - u_0^4(2u_h^4 + \Omega^2 b_0^2))}{u_0(u_0^4 - u_h^4)(3(u_0^8 + u_h^8) + u_0^4(2u_h^4 - \Omega^2 b_0^2))}(u - u_0), \\ b(u) &= b_0 - \frac{b_0 u_0 \Omega^2 (u_0^4 + u_h^4)^2}{(u_0^4 - u_h^4)(3(u_0^8 + u_h^8) + u_0^4(2u_h^4 - \Omega^2 b_0^2))}(u - u_0) \end{aligned} \quad (\text{A.19})$$

where now $b_0 = b(u = u_0)$. BH embeddings and Minkowski embeddings are separated by the critical solution, for which $u_0 \rightarrow u_c$. It can be expanded as

$$\begin{aligned}\psi(u) &= 1 - \frac{4(u_c^4 + u_h^4) + \Omega^2 u_c^2}{2u_c^2(u_c^4 + u_h^4)}(u - u_c)^2, \\ b(u) &= \frac{u_c^4 - u_h^4}{\Omega u_c^2} - \frac{\Omega}{2u_c}(u - u_c).\end{aligned}\tag{A.20}$$

Finally, suppose we would like to fix boundary conditions at the background black hole horizon. Setting

$$\begin{aligned}\psi(u) &= \psi_0^{BH} + \psi_1^{BH}(u - u_h) + \dots \\ b(u) &= b_0^{BH} + b_1^{BH}(u - u_h) + \dots\end{aligned}$$

we can insert this expansion into (A.14) and find

$$\chi'(u) = \frac{\Omega}{4u_h} \sqrt{2 + (b_1^{BH})^2 + \frac{2u_h^2(\psi_1^{BH})^2}{1 - (\psi_0^{BH})^2}} \frac{1}{u - u_h} + \mathcal{O}(u - u_h)^0 + \dots\tag{A.21}$$

which exhibits a logarithmic divergence of $\chi(u)$ close to the background black hole horizon.

B Holographic dictionary

Let us begin by writing the euclidean on-shell action as

$$\mathcal{I}_{\text{bulk}} = \int_{u_{\min}}^{u_{\max}} du \mathcal{L}(\psi, \psi', c, c', \bar{c}, \bar{c}')\tag{B.1}$$

where

$$\mathcal{L} = \sqrt{(1 - \psi^2) \left(\left[u^4 g(u)^2 |c'|^2 - \Omega^2 \Re(c\bar{c}') \right] (1 - \psi^2) + h(u) \left[u^4 g(u)^2 - \Omega^2 |c|^2 \right] (1 - \psi^2 + u^2 \psi'^2) \right)}\tag{B.2}$$

with primes denoting derivatives with respect to the radial coordinate u and $u_{\min} = u_c$ (u_0) for BH (Minkowski) embeddings. In (B.1) we have absorbed the factors corresponding to the integrations over the worldsheet coordinates different from the holographic coordinate u . Evaluating this action with the UV expansion (2.14) we find, for large u ,

$$\mathcal{I}_{\text{bulk}} \sim \int_{u_{\min}}^{u_{\max}} du \left(u^2 - \frac{m^2}{2} \right)\tag{B.3}$$

which is divergent when $u_{\max} \rightarrow \infty$. Here $u_{\min} = u_h$ (u_0) for BH (Minkowski) embeddings. The electric field does not introduce any new divergences, so the counterterms are [41]

$$\begin{aligned}L_1 &= -\frac{1}{3}\sqrt{\gamma} \\ L_2 &= \frac{1}{2}\sqrt{\gamma} \arcsin^2 \psi\end{aligned}\tag{B.4}$$

where γ is the determinant of the induced metric at some regulator surface $u = u_{\max}$

$$\sqrt{\gamma} = u_{\max}^3 g(u_{\max}) \sqrt{h(u_{\max})} = u_{\max}^3 \left(1 - \frac{u_h^4}{u_{\max}^4}\right) \sqrt{1 + \frac{u_h^4}{u_{\max}^4}} \quad (\text{B.5})$$

Then, evaluating the boundary contribution of $L_1 + L_2$, we get the boundary action $\mathcal{I}_{\text{bdry}}$ with the UV expansion

$$\begin{aligned} \mathcal{I}_{\text{bdry}} &= u_{\max}^3 \left(1 - \frac{u_h^4}{u_{\max}^4}\right) \sqrt{1 + \frac{u_h^4}{u_{\max}^4}} \left(-\frac{1}{3} + \frac{1}{2} \arcsin^2 \psi\right) \\ &= -\frac{u_{\max}^3}{3} + \frac{m^2}{2} u_{\max} + m\mathcal{C}. \end{aligned} \quad (\text{B.6})$$

For convenience, rewrite

$$u_{\max}^3 = \int_{u_{\min}}^{u_{\max}} 3u^2 du + u_{\min}^3, \quad u_{\max} = \int_{u_{\min}}^{u_{\max}} du + u_{\min}.$$

Then the total action $\mathcal{I} = \mathcal{I}_{\text{bulk}} + \mathcal{I}_{\text{bdry}}$ can be written as

$$\mathcal{I} = \int_{u_{\min}}^{u_{\max}} du \left[\mathcal{L}(u) - u^2 + \frac{m^2}{2} \right] - \frac{u_{\min}^3}{3} + \frac{m^2}{2} u_{\min} + m\mathcal{C}. \quad (\text{B.7})$$

Let us consider the variations of this action. On shell, the variation of the bulk part on shell gives only boundary contributions

$$\delta\mathcal{I}_{\text{bulk}} = \left[\frac{\partial\mathcal{L}}{\partial\psi'} \delta\psi + \frac{\partial\mathcal{L}}{\partial c'} \delta c + \frac{\partial\mathcal{L}}{\partial \bar{c}'} \delta \bar{c} \right] \Big|_{u_{\min}}^{u_{\max}}.$$

Let us insert the Taylor expansions (2.13)(2.14) around both u_{\max} and u_{\min}

$$\begin{aligned} \left[\frac{\partial\mathcal{L}}{\partial\psi'} \delta\psi + \frac{\partial\mathcal{L}}{\partial c'} \delta c + \frac{\partial\mathcal{L}}{\partial \bar{c}'} \delta \bar{c} \right] \Big|_{u_{\max}}^{u_{\max}} &= -m\delta\mathcal{C} - 2\mathcal{C}\delta m - m u_{\max} \delta m - \vec{j} \cdot \delta \vec{A} + \mathcal{O}(u_{\max}^{-1}), \\ \left[\frac{\partial\mathcal{L}}{\partial\psi'} \delta\psi + \frac{\partial\mathcal{L}}{\partial c'} \delta c + \frac{\partial\mathcal{L}}{\partial \bar{c}'} \delta \bar{c} \right] \Big|_{u_{\min}}^{u_{\min}} &= -\frac{q}{\Omega} \delta\chi_0, \end{aligned} \quad (\text{B.8})$$

where we have written the contribution at u_{\min} in its most compact form, i.e. in terms of the phase χ_0 at the horizon.

Moreover, the variation of the boundary term (B.6) can be immediately obtained

$$\delta\mathcal{I}_{\text{bdry}} = m u_{\max} \delta m + m \delta\mathcal{C} + \mathcal{C} \delta m \quad (\text{B.9})$$

Then, the variation of \mathcal{I} becomes:

$$\delta\mathcal{I} = -\mathcal{C}\delta m - \vec{j} \cdot \delta \vec{A} - \frac{q}{\Omega} \delta\chi_0. \quad (\text{B.10})$$

Basically there are two choices in the literature for the IR cutoff, $u_{\min} = u_h$ (the background horizon) or $u_{\min} = u_c$, the critical surface. The problem with the first choice is that the phase χ diverges logarithmically as $\log(u - u_h)$. This is the counterpart of the divergence

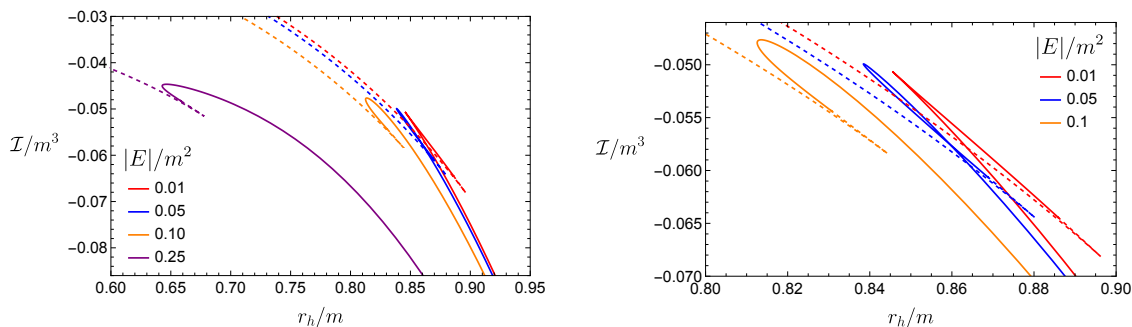


Figure 12. On-shell Euclidean action for different values of the electric field. Solid (dashed) lines correspond to BH (Minkowski) embeddings.

in A_x that appears in the case of a constant electric field in the x direction [23]. The second choice gives an IR regulator that has been considered by several authors [19, 42, 43]. Adhering to this second option, since χ is well defined in all its range, and is so up to a global shift, we can always arrange its variation to vanish at the horizon $\delta\chi_0 = 0$. With this convention, we get

$$\delta\mathcal{I} = \delta\mathcal{I}_{\text{bulk}} + \delta\mathcal{I}_{\text{bdry}} = -\mathcal{C}\delta m - \vec{j} \cdot \delta\vec{A}. \tag{B.11}$$

This expression confirms the consistency of the holographic dictionary for our model, that is, that the 1-point functions \mathcal{C} and \vec{j} are obtained from the functional variation of the on-shell action with respect to the sources m and \vec{A} . This has been checked explicitly for the analytic massless solution in appendix D. By considering a family of solutions $\{\psi(u), c(u), \bar{c}(u)\}$, parametrized by ψ_0 , the insertion angle at the singular shell, and adjusting $c(u_c), \bar{c}(u_c)$ such as to keep $|E|/m^2$ constant at the boundary we can integrate $\mathcal{I}(\psi_0) = -\int_0^{\psi_0} [\mathcal{C}(\psi)m'(\psi) + \vec{j}(\psi) \cdot \vec{A}'(\psi)] d\psi$ and obtain the plots as shown in figure 12.

These plots coincide with the direct evaluation of the Euclidean action in this family of solutions. We see that only for very weak electric field does the curve look like the typical one of first order phase transitions. However as soon as $|E|/m^2$ increases we find a behaviour that departs from the typical swallow tail curve. This is not cured if we extend the domain of u until $u_{\text{min}} = u_h$. We see that the problems appear in the black hole (unstable) branch. This casts doubt on the interpretation of the euclidean on shell action as a free energy. In particular the disappearance of the cusp would imply a negative value of the entropy (see appendix C in [44]).

C Effective horizon and effective temperature

Let h_{ab} be the induced six-dimensional metric and \mathcal{F}_{ab} the worldvolume gauge field. The effective open string metric γ_{ab} is defined as

$$\gamma_{ab} = h_{ab} + (2\pi\alpha')^2 \mathcal{F}_{ac} \mathcal{F}_{bd} h^{cd}. \tag{C.1}$$

In order to write the form of this metric for our ansatz when the embedding is parameterized as a function $\psi = \psi(u)$, let us define the function $F(u)$ as:

$$F(u) \equiv \left(u^2 g^2 - \frac{\Omega^2 |c|^2}{u^2} \right) \frac{1}{h}, \quad (\text{C.2})$$

and the complex one-forms e_{\pm} as:

$$e_{\pm} = e^{\mp i\Omega t} (dx \pm idy). \quad (\text{C.3})$$

Then, we have

$$\begin{aligned} \gamma_{ab} d\xi^a d\xi^b = & -F(u) dt^2 + \left[\frac{1}{u^2} + \frac{\psi'^2}{1-\psi^2} + \frac{|c'|^2}{u^2 h} \right] du^2 + \frac{2}{u h} \text{Im}(c \bar{c}') dt du + \\ & + \frac{1}{4} \left[\frac{1}{u^2} + \frac{\psi'^2}{1-\psi^2} \right]^{-1} (e_- c' + e_+ \bar{c}')^2 + \frac{\Omega^2}{4} \frac{h}{u^2 g^2} (e_- c + e_+ \bar{c})^2 + \frac{h^2 F(u)}{g^2} e_+ e_-, \end{aligned} \quad (\text{C.4})$$

where $c = b e^{i\chi}$ is the complexified field potential in the rotating frame. In order to diagonalize the (t, u) part of the metric (C.4), let us define new coordinates (τ, u_*) as

$$d\tau = dt - A(u) du, \quad du_* = B(u) du, \quad (\text{C.5})$$

where $A(u)$ and $B(u)$ are given by:

$$A(u) = \frac{\Omega b^2 \chi'}{u^2 h F}, \quad B(u) = \frac{\mathcal{L}}{u^2 h (1 - \psi^2) F}, \quad (\text{C.6})$$

and \mathcal{L} is the lagrangian density (A.12). In these new coordinates the effective open string metric takes the form:

$$\begin{aligned} \gamma_{ab} d\xi^a d\xi^b = & F(u) (-d\tau^2 + du_*^2) + \frac{1}{4} \left[\frac{1}{u^2} + \frac{\psi'^2}{1-\psi^2} \right]^{-1} (e_- c' + e_+ \bar{c}')^2 + \\ & + \frac{\Omega^2}{4} \frac{h}{u^2 g^2} (e_- c + e_+ \bar{c})^2 + \frac{h^2 F(u)}{g^2} e_+ e_-. \end{aligned} \quad (\text{C.7})$$

The function $F(u)$ vanishes at $u = u_c$ (where $|c| = (u_c^4 - u_h^4)/(\Omega u_c^2) = b_0$). Thus, $u = u_c$ is an event horizon for the effective metric. The corresponding Hawking temperature can be obtained from the surface curvature at $u = u_c$, namely:

$$T_{\text{eff}} = - \frac{\gamma'_{tt}}{4\pi \gamma_{tu}} \Big|_{u=u_c}. \quad (\text{C.8})$$

From the values of γ_{tt} and γ_{tu} found above, we can readily demonstrate that:

$$T_{\text{eff}} = \frac{2u_c h(u_c) - \Omega b_1}{2\pi b_0 \chi_1} = \frac{\Omega}{2\pi \chi_1 u_c g(u_c)} \left[2h(u_c) - \frac{\Omega b_1}{u_c} \right], \quad (\text{C.9})$$

where b_0 , b_1 and χ_1 are the coefficients defined in (A.16) for black hole embeddings.

D Analytic solutions

When the mass parameter m is zero or small it is possible to find analytic solutions of the equations of motion. These solutions are much easier to find in the angular coordinates (r, θ) defined in (A.1) and (A.6) with $\theta = \theta(r)$. It is straightforward to prove that the lagrangian density with this parameterization is:

$$\mathcal{L} = \frac{\cos^2 \theta}{\sqrt{r^4 - r_h^4}} \sqrt{(r^4 - r_h^4 - \Omega^2 b^2) ((r^4 - r_h^4) (b'^2 + r^2 \theta'^2) + r^4) + b^2 (r^4 - r_h^4)^2 \chi'^2}. \quad (\text{D.1})$$

Moreover, the cyclic coordinate χ is now related to $\theta(r)$ and $b(r)$ as:

$$\chi'(r) = \frac{q \sqrt{r^4 - r_h^4 - \Omega^2 b^2} \sqrt{(r^4 - r_h^4) (b'^2 + r^2 \theta'^2) + r^4}}{b (r^4 - r_h^4) \sqrt{b^2 \Omega^2 (r^4 - r_h^4) \cos^4 \theta - q^2}}. \quad (\text{D.2})$$

The Routhian that is obtained after eliminating χ' from \mathcal{L} is:

$$\mathcal{R} = \frac{\sqrt{(r^4 - r_h^4) (b'^2 + r^2 \theta'^2) + r^4}}{\Omega b (r^4 - r_h^4)} \sqrt{r^4 - r_h^4 - \Omega^2 b^2} \sqrt{\Omega^2 b^2 (r^4 - r_h^4) \cos^4 \theta - q^2}. \quad (\text{D.3})$$

The tortoise coordinates in this (τ, r_*) parameterization are defined as

$$d\tau = dt - A_\theta(r) dr, \quad dr_* = B_\theta(r) dr, \quad (\text{D.4})$$

where $A_\theta(r)$ and $B_\theta(r)$ are the following functions:

$$A_\theta(r) = \frac{\Omega b^2 \chi'}{r^4 - r_h^4 - b^2 \Omega^2}, \quad B_\theta(r) = \frac{\mathcal{L}}{\cos^2 \theta (r^4 - r_h^4 - b^2 \Omega^2)}, \quad (\text{D.5})$$

with \mathcal{L} being the lagrangian density (D.1). In terms of (τ, r_*) the (t, r) part of the effective metric takes the form

$$\frac{r^4 - r_h^4 - b^2 \Omega^2}{r^2} (-d\tau^2 + dr_*^2), \quad (\text{D.6})$$

which means that, indeed, these new coordinates are tortoise coordinates for the effective open string metric.

D.1 Massless solution

Let us now consider a massless embedding with $\theta = 0$. The Routhian (D.3) for this case takes the form:

$$\mathcal{R}_0 = \frac{\sqrt{(r^4 - r_h^4) b'^2 + r^4} \sqrt{[\Omega^2 b^2 - r^4 + r_h^4] [\Omega^2 b^2 (r^4 - r_h^4) - q^2]}}{\Omega b (r^4 - r_h^4)}. \quad (\text{D.7})$$

Both factors in the second square root in (D.7) must vanish simultaneously at the pseudo-horizon r_c in order to keep the Routhian real. From this condition, we get:

$$b_0^2 = \frac{q}{\Omega^2} = \frac{r_c^4 - r_h^4}{\Omega^2}, \quad (\text{D.8})$$

where, in the second step, we have used that $q = r_c^4 - r_h^4$ for the massless embeddings. Actually, one can verify from the equation of motion of R_0 that $b = b_0$ is a solution of this equation in which b is constant. Moreover, plugging $b = b_0$ into the right-hand side of (D.2), we get that the phase $\chi(r)$ in this massless case satisfies

$$\chi'_{m=0} = \Omega \frac{r^2}{r^4 - r_h^4} = \frac{\Omega}{r^2 f(r)}. \quad (\text{D.9})$$

In order to write explicitly the function $\chi_{m=0}(r)$, let us define a new function $\Lambda(x)$ as:

$$\Lambda(x) \equiv \log \frac{x-1}{x+1} - 2 \operatorname{arccot} x, \quad \frac{d\Lambda}{dx} = \frac{4x^2}{x^4 - 1}. \quad (\text{D.10})$$

One has:

$$\chi_{m=0}(r) = \frac{\Omega}{4r_h} \Lambda(r/r_h), \quad (\text{D.11})$$

where we have fixed the integration constant in such a way that $\Lambda(x) \rightarrow 0$ for $x \rightarrow \infty$ ($\Lambda(x) \approx -4/x$ for large x). Therefore, the complexified gauge potential $c(r) = b_0 e^{i\chi_{m=0}(r)}$ in the rotating wave frame is:

$$c(r) = \frac{\sqrt{r_c^4 - r_h^4}}{\Omega} e^{\frac{i\Omega}{4r_h} \Lambda(r/r_h)}. \quad (\text{D.12})$$

By expanding the right-hand side of (D.12) for large r and comparing the result with (2.14), we get the electric field E and the current j , namely:

$$E = j = -i\sqrt{r_c^4 - r_h^4} = -i\sqrt{q}. \quad (\text{D.13})$$

Thus, E and j are parallel and equal, which corresponds to $\gamma_{xx} = 1$ and $\gamma_{xy} = 0$ in the conductivity tensor. Using (2.15) it is easy to derive the correctly normalised physical conductivity, relating the physical electric field and the physical current, as

$$\sigma(\Omega) = \frac{\sqrt{2} N_f N_c}{\pi \sqrt{\lambda}}.$$

Up to a convention factor of $\sqrt{2}$ this result matches the one obtained in [11], (see eq. (5.8)), were the observation is made that this conductivity is nothing else than $1/g^2$ in terms of the effective defect field theory gauge coupling on the D5-brane. This normalisation should affect all the conductivities obtained previously in this paper. Importantly, our result also agrees with the findings in [12] in that the response of the system is not only linear, but instantaneous.

The effective temperature in angular coordinates is given by:

$$T_{\text{eff}} = \frac{1}{2\pi} \frac{2r_c^3 - b_0 b_1 \Omega^2}{\Omega b_0^2 \chi_1}, \quad (\text{D.14})$$

where $b_1 = b'(r = r_c)$ and $\chi_1 = \chi'(r = r_c)$. In the massless solution found above $b_1 = 0$ and the value of χ_1 can be read from (D.9) by taking $r = r_c$. We get:

$$T_{\text{eff}} = \frac{r_c}{\pi} = \frac{(q + r_h^4)^{\frac{1}{4}}}{\pi}. \quad (\text{D.15})$$

We can now insert the massless solution into the renormalized action \mathcal{I} and check our general equation (B.10). Indeed, for a massless solution, the renormalized euclidean action can be written as:

$$\mathcal{I}(m = 0) = \mathcal{J}(r_c) - \frac{r_c^3}{3}, \tag{D.16}$$

where $\mathcal{J}(r_c)$ is the following integral in the r coordinate:

$$\mathcal{J}(r_c) = \int_{r_c}^{\infty} dr r^2 \left(\sqrt{1 - \frac{\Omega^2}{r^2 f} |c|^2 + r^2 |c'|^2 - \frac{\Omega^2}{r_h^2} (\text{Re}(\bar{c}c'))^2} - 1 \right). \tag{D.17}$$

By using the explicit form (D.12) of the complexified gauge potential $c(r)$ for the massless solution, one can easily demonstrate that the integral $\mathcal{J}(r_c)$ vanishes on-shell. Therefore, the renormalized on-shell action in this case is simply:

$$\mathcal{I}(m = 0) \Big|_{\text{on-shell}} = -\frac{r_c^3}{3}. \tag{D.18}$$

Let us now make use of this last expression to verify our general formula for the variation of the on-shell action in this massless case. In terms of the complexified gauge potential at the UV, the general variation of the renormalized on-shell action for $m = 0$ takes the form:

$$\delta \mathcal{I}(m = 0) \Big|_{\text{on-shell}} = -\frac{1}{2} \bar{j} \delta c_{uv}(r_c) - \frac{1}{2} j \delta \bar{c}_{uv}(r_c) - \frac{q}{\Omega} \delta \chi_0(r_c). \tag{D.19}$$

Notice that we have included the variation of the phase χ at $r = r_c$, which is non-zero with the conventions used in this appendix.³ It is now straightforward to find the values of c_{uv} and χ_0 for the solution (D.12), namely:

$$c_{uv} = \frac{\sqrt{r_c^4 - r_h^4}}{\Omega}, \quad \chi_0(r_c) = \frac{\Omega}{4r_h} \Lambda(r_c/r_h). \tag{D.21}$$

Their contribution to the right-hand side of (D.19) is

$$-\frac{1}{2} \bar{j} \delta c_{uv}(r_c) - \frac{1}{2} j \delta \bar{c}_{uv}(r_c) = 0, \quad \delta \chi_0(r_c) = \frac{\Omega}{r_c^4 - r_h^4} r_c^2 \delta r_c, \tag{D.22}$$

where we used the value of j displayed in (D.13). Taking into account that $q = r_c^4 - r_h^4$, we get:

$$\delta \mathcal{I}(m = 0) \Big|_{\text{on-shell}} = -\frac{q}{\Omega} \delta \chi_0(r_c) = -r_c^2 \delta r_c, \tag{D.23}$$

which is, indeed, the first variation of (D.18).

³Alternatively, we could have integrated (D.9) by imposing the vanishing of the phase χ at $r = r_c$. The complexified gauge potential in this case would be:

$$c(r) = \frac{\sqrt{r_c^4 - r_h^4}}{\Omega} e^{\frac{i\Omega}{4r_h} [\Lambda(r/r_h) - \Lambda(r_c/r_h)]}. \tag{D.20}$$

With this convention the last term in (D.19) does not contribute to the variation of the on-shell action.

D.2 Small mass solutions

Let us now consider small mass solutions in which $b(r)$ and $\theta(r)$ are given by:

$$b(r) = b_0 + \beta(r), \quad \theta(r) = \lambda(r), \quad (\text{D.24})$$

where the functions $\beta(r)$ and $\lambda(r)$ are small. At first order in these functions, they satisfy the following linear equations of motion:

$$\begin{aligned} \frac{d}{dr} [(r^4 f - q) \lambda'] + 2r^2 \lambda &= 0, \\ \frac{d}{dr} \left[\frac{r^4 f - q}{r^2} \beta' \right] + \frac{4r^2 \Omega^2}{r^4 f - q} \beta &= 0, \end{aligned} \quad (\text{D.25})$$

which can be written as:

$$\begin{aligned} (r^4 - r_c^4) \lambda'' + 4r^3 \lambda' + 2r^2 \lambda &= 0, \\ r^2 (r^4 - r_c^4) \beta'' + 2r (r^4 + r_c^4) \beta' + 4\Omega^2 \frac{r^6}{r^4 - r_c^4} \beta &= 0. \end{aligned} \quad (\text{D.26})$$

These equations are equivalent to those solved in appendix B of [1] and, therefore, we can just adapt the results in [1] to our case. Let us start by writing the general solution for the differential equation satisfied by $\lambda(r)$:

$$\lambda(r) = c_1 F\left(\frac{1}{4}, \frac{1}{2}; \frac{3}{4}; \frac{r^4}{r_c^4}\right) + c_2 r F\left(\frac{1}{2}, \frac{3}{4}; \frac{5}{4}; \frac{r^4}{r_c^4}\right), \quad (\text{D.27})$$

where c_1 and c_2 are constants. Imposing regularity conditions as in [1], we find that the integration constants c_1 and c_2 must satisfy the relation:

$$\frac{c_1}{c_2} = -\frac{r_c}{4} \frac{\left[\Gamma\left(\frac{1}{4}\right)\right]^2}{\left[\Gamma\left(\frac{3}{4}\right)\right]^2} = -\frac{r_c}{4} \frac{\sqrt{2} \Gamma\left(\frac{5}{4}\right)}{\left[\Gamma\left(\frac{3}{4}\right)\right]^3} \quad (\text{D.28})$$

Let us write the UV behavior of $\theta(r)$ as:

$$\theta(r) \approx \frac{m}{r} + \frac{\mathcal{C}}{r^2} + \dots, \quad (r \rightarrow \infty), \quad (\text{D.29})$$

where m and \mathcal{C} are the mass and condensate parameters respectively. They are related to c_1 and c_2 as:

$$\begin{aligned} m &= r_c c_1 \frac{\Gamma\left(\frac{3}{4}\right) \Gamma\left(\frac{1}{4}\right)}{\sqrt{2} \pi} = r_c c_1 \\ \mathcal{C} &= -r_c^3 c_2 \frac{\Gamma\left(\frac{5}{4}\right) \Gamma\left(-\frac{1}{4}\right)}{\sqrt{2} \pi} = r_c^3 c_2. \end{aligned} \quad (\text{D.30})$$

It follows that \mathcal{C} and m are linearly related in this small mass solutions:

$$\mathcal{C} = -r_c \left[\frac{2 \Gamma\left(\frac{3}{4}\right)}{\Gamma\left(\frac{1}{4}\right)} \right]^2 m. \quad (\text{D.31})$$

Moreover, the function $\theta(r)$ can be written as:

$$\theta(r) = \frac{m}{r_c} F\left(\frac{1}{4}, \frac{1}{2}; \frac{3}{4}; \frac{r^4}{r_c^4}\right) + \frac{C}{r_c^3} r F\left(\frac{1}{2}, \frac{3}{4}; \frac{5}{4}; \frac{r^4}{r_c^4}\right). \quad (\text{D.32})$$

Let us next look at the equation satisfied by the gauge field perturbation $\beta(r)$ in the system (D.26). Its general solution is:

$$\beta(r) = d \exp\left[-\frac{i\Omega}{2r_c} \Lambda(r/r_c)\right] + \bar{d} \exp\left[\frac{i\Omega}{2r_c} \Lambda(r/r_c)\right], \quad (\text{D.33})$$

where d is a complex constant. It is interesting to find the solution for the complex potential $c = be^{i\chi}$. For the massless solution $c(r)$ takes the value:

$$c_0(r) = b_0 e^{i\chi_{m=0}(r)} = b_0 e^{\frac{i\Omega}{4r_h} \Lambda(r/r_h)}. \quad (\text{D.34})$$

Let us denote

$$\delta c(r) \equiv c(r) - c_0(r). \quad (\text{D.35})$$

This function satisfies the following differential equation at linear order:

$$r(r^4 - r_c^4)(r^4 - r_h^4)^2 \delta c'' + 2(r^4 - r_h^4)[r^8 + (r_c^4 - r_h^4)r^3(r + i\Omega) - r_c^4 r_h^4] \delta c' + r^5 \Omega [\Omega r^4 + (r_c^4 - 2r_h^4)\Omega - 4i(r_c^4 - r_h^4)r] \delta c = 0 \quad (\text{D.36})$$

Instead of trying to solve directly this equation we notice that δc , at first order, can be written as:

$$\delta c = e^{i\chi_{m=0}(r)} (\beta + i b_0 \delta \chi), \quad (\text{D.37})$$

where $\delta \chi(r) = \chi(r) - \chi_{m=0}(r)$. The equation satisfied by $\delta \chi(r)$ is rather simple, namely:

$$\delta \chi' = -\frac{2r^2 \Omega}{b_0 (r^4 - r_c^4)} \beta, \quad (\text{D.38})$$

and can be readily integrated:

$$\delta \chi(r) = -\frac{id}{b_0} \exp\left[-\frac{i\Omega}{2r_c} \Lambda(r/r_c)\right] + \frac{i\bar{d}}{b_0} \exp\left[\frac{i\Omega}{2r_c} \Lambda(r/r_c)\right] + \varphi, \quad (\text{D.39})$$

where φ is a constant. Plugging (D.33) and (D.39) into (D.37), we obtain:

$$\delta c(r) = A \exp\left[i\frac{\Omega}{4}\left(\frac{1}{r_h} \Lambda(r/r_h) - \frac{2}{r_c} \Lambda(r/r_c)\right)\right] + B \exp\left[\frac{i\Omega}{4r_h} \Lambda(r/r_h)\right], \quad (\text{D.40})$$

where $A = 2d$ and $B = i\frac{\varphi}{\Omega} \sqrt{r_c^4 - r_h^4}$. To proceed further we have to impose a regularity condition to the general solution (D.40). With this purpose let us write $\delta c(r)$ in terms of the tortoise coordinates (D.4) for the open string metric. In this massless case it is easy to demonstrate that (D.4) can be integrated to give the following relation between the tortoise coordinates (τ, r_*) and our original coordinates (t, r) :

$$\tau = t + \frac{1}{4r_h} \Lambda\left(\frac{r}{r_h}\right) - r_*, \quad r_* = \frac{1}{4r_c} \Lambda\left(\frac{r}{r_c}\right). \quad (\text{D.41})$$

The new radial coordinate r_* varies from $r_* = -\infty$ at the pseudohorizon to $r_* = 0$ at the UV boundary. Actually, one can prove that in these regions it can be related to r as

$$r_* = -\frac{1}{r} + \mathcal{O}(r^{-5}), \quad (r \rightarrow \infty), \quad r_* \sim \frac{1}{4r_c} \log(r - r_c), \quad (r \rightarrow r_c). \quad (\text{D.42})$$

Let us next consider the time-dependent gauge potential $\delta a(r, t)$, given by:

$$\delta a(r, t) = \delta c(r) e^{i\Omega t}. \quad (\text{D.43})$$

By combining (D.40) and (D.41) it straightforward to prove that δa can be written in terms of (τ, r_*) simply as:

$$\delta a(\tau, r_*) = A e^{i\Omega(\tau - r_*)} + B e^{i\Omega(\tau + r_*)}. \quad (\text{D.44})$$

We next impose an infalling boundary condition, which amounts to select the solutions with $A = 0$ in (D.44). Therefore, the regular solutions we are looking for are:

$$\delta a(\tau, r_*) = B e^{i\Omega(\tau + r_*)}. \quad (\text{D.45})$$

Equivalently, $\delta c(r)$ is given by:

$$\delta c(r) = B \exp \left[\frac{i\Omega}{4r_h} \Lambda(r/r_h) \right]. \quad (\text{D.46})$$

We can now read off the electric field and current from the asymptotic behaviour of δc , namely:

$$\delta c(r) \approx B - \frac{i\Omega B}{r} + \dots, \quad (r \rightarrow \infty). \quad (\text{D.47})$$

Thus, we have

$$\delta E = \delta j = -i\Omega B, \quad (\text{D.48})$$

which means that the equality of E and j of the massless solution is maintained at first order in these small mass solutions.

E Photovoltaic conductivities

In order to study the photovoltaic current of the model the proposal in [26] is to analyze the response of our system to an additional linearly polarized electric field on top of the circularly driven background (2.4). In vector cartesian notation, the total electric field is now

$$\vec{\mathcal{E}}(t) = O(t)\vec{E} + \vec{\epsilon}(t) = O(t)\vec{E} + \vec{\epsilon} e^{-i\omega t}, \quad (\text{E.1})$$

where ϵ is a constant vector such that $|\vec{\epsilon}| \ll |\vec{E}|$. We want to extract the effective conductivities that arise from the effect of this perturbation on the current. The perturbation of the electric field will also mean a change in the gauge potential $\vec{a} + \delta\vec{a}$, so that $c(r)$ develops a time dependent perturbation

$$\vec{a}(t, r) + \delta\vec{a}(t, r) = O(t) \left(\vec{c}(r) + \delta\vec{c}(t, r) \right). \quad (\text{E.2})$$

Now the bulk gauge potential $\vec{a}(t, r) + \delta\vec{a}(t, r)$ has to match the full electric field at the boundary

$$\vec{a}(t, r = \infty) + \delta\vec{a}(t, r = \infty) = -\frac{1}{\Omega} O(t) \boldsymbol{\varepsilon} \vec{E} - \frac{i}{\omega} \vec{\epsilon} e^{-i\omega t}. \quad (\text{E.3})$$

Since the fluctuations of the gauge field will also couple to the embedding functions $\theta(r) \rightarrow \theta(r) + \delta\theta(t, r)$ we will be dealing with a 3 component vector of fluctuations $\delta\vec{\xi}(t, \rho) = (\delta c_x, \delta c_y, \delta\theta)$. The general formalism to study these fluctuations has been developed in [1], following the analysis of [9] for the massless D3-D7 system. In this appendix we will summarize this method. First of all, let us write the perturbed equations in terms of the tortoise coordinates (τ, r_*) defined in (D.4). We get:

$$(\partial_\tau^2 - \partial_{r_*}^2 + \mathbf{A}(r) \partial_\tau + \mathbf{B}(r) \partial_{r_*} + \mathbf{C}(r)) \delta\vec{\xi} = 0, \quad (\text{E.4})$$

where A, B and C are 3×3 matrices which at the pseudohorizon $r = r_c$ satisfy

$$\mathbf{A}(r = r_c) = -\mathbf{B}(r = r_c) \equiv \mathbf{A}_c \quad \mathbf{C}(r = r_c) = 0. \quad (\text{E.5})$$

Thus, in this limit, which correspond to $r_* \rightarrow -\infty$, the fluctuation equation (E.4) becomes

$$(\partial_\tau^2 - \partial_{r_*}^2) \delta\vec{\xi} + \mathbf{A}_c (\partial_\tau - \partial_{r_*}) \delta\vec{\xi} = 0, \quad (\text{E.6})$$

whose general solution takes the form

$$\delta\vec{\xi} = \vec{f}(\tau + r_*) + e^{-\mathbf{A}_c r_*} \vec{g}(\tau - r_*). \quad (\text{E.7})$$

We will impose that $\vec{g} = 0$, which selects the ingoing wave boundary condition at the pseudohorizon. Let us next look at the UV boundary condition (E.3). First of all, we rewrite the rotation matrix $O(t)$ as:

$$O(t) = \mathbf{M}_+ e^{i\Omega t} + \mathbf{M}_- e^{-i\Omega t}, \quad (\text{E.8})$$

where

$$\mathbf{M}_\pm = \frac{1}{2} \begin{pmatrix} 1 & \pm i \\ \mp i & 1 \end{pmatrix}. \quad (\text{E.9})$$

Then, defining the frequencies $\omega_\pm = \omega \pm \Omega$, the boundary UV condition of $\delta\vec{c}$ can be written as

$$\delta\vec{c}(t, r = \infty) = -\frac{i}{\omega} \left(\mathbf{M}_+ e^{-i\omega_+ t} + \mathbf{M}_- e^{-i\omega_- t} \right) \vec{\epsilon}. \quad (\text{E.10})$$

Let us assume that $\delta\vec{c}(t, r)$ and $\delta\theta(t, r)$ oscillate with frequencies ω_\pm

$$\delta\vec{c}(t, r) = \vec{\beta}_+(r) e^{-i\omega_+ t} + \vec{\beta}_-(r) e^{-i\omega_- t}, \quad \delta\theta(t, r) = \gamma_+(r) e^{-i\omega_+ t} + \gamma_-(r) e^{-i\omega_- t}. \quad (\text{E.11})$$

Then, our system of equations (E.4) for the fluctuations becomes

$$\left[\frac{d^2}{dr_*^2} - \mathbf{B}(r) \frac{d}{dr_*} + \omega_\pm^2 + i\omega_\pm \mathbf{A}(r) - \mathbf{C}(r) \right] \vec{\xi}_\pm = 0. \quad (\text{E.12})$$

Let us write the boundary expansions for the fields in the form

$$\delta\vec{c}(t, r) \approx \delta\vec{c}^{(0)}(t) + \frac{\delta\vec{c}^{(1)}(t)}{r} + \dots, \quad \vec{\beta}_{\pm}(r) = \vec{\beta}_{\pm}^{(0)} + \frac{\vec{\beta}_{\pm}^{(1)}}{r} + \dots \quad (\text{E.13})$$

Plugging these expansions in (E.11) we get

$$\delta\vec{c}^{(0)}(t) = \vec{\beta}_{+}^{(0)} e^{-i\omega_+ t} + \vec{\beta}_{-}^{(0)} e^{-i\omega_- t}, \quad \delta\vec{c}^{(1)}(t) = \vec{\beta}_{+}^{(1)} e^{-i\omega_+ t} + \vec{\beta}_{-}^{(1)} e^{-i\omega_- t}. \quad (\text{E.14})$$

Comparing the first of these equations with (E.10) we conclude that

$$\vec{\beta}_{\pm}^{(0)} = -\frac{i}{\omega} \mathbf{M}_{\pm} \vec{\epsilon}. \quad (\text{E.15})$$

The subleading vectors $\vec{\beta}_{\pm}^{(1)}$ determine the variation of the current $\delta\vec{\mathcal{J}}(t) = O(t) \delta\vec{c}^{(1)}(t)$, namely:

$$\delta\vec{\mathcal{J}}(t) = e^{-i\omega t} \left(\mathbf{M}_{+} \vec{\beta}_{+}^{(1)} + \mathbf{M}_{-} \vec{\beta}_{-}^{(1)} + \mathbf{M}_{+} \vec{\beta}_{-}^{(1)} e^{2i\Omega t} + \mathbf{M}_{-} \vec{\beta}_{+}^{(1)} e^{-2i\Omega t} \right). \quad (\text{E.16})$$

For a regular solution the vectors $\vec{\beta}_{\pm}^{(1)}$ and $\vec{\beta}_{\pm}^{(0)}$ are related. Let us write this relation as

$$\vec{\beta}_{\pm}^{(1)} = \mathbf{X}_{\pm} \vec{\beta}_{\pm}^{(0)} = -\frac{i}{\omega} \mathbf{X}_{\pm} \mathbf{M}_{\pm} \vec{\epsilon}, \quad (\text{E.17})$$

where \mathbf{X}_{\pm} are 2×2 matrices that, in general, must be determined numerically (see [1] for details). Plugging (E.17) into (E.16) we get a relation between the current $\delta\vec{\mathcal{J}}$ and the applied electric field $\vec{\epsilon}$

$$\delta\vec{\mathcal{J}} = \left[\boldsymbol{\sigma}(\omega) e^{-i\omega t} + \boldsymbol{\sigma}^{+}(\omega) e^{-i(\omega+2\Omega)t} + \boldsymbol{\sigma}^{-}(\omega) e^{-i(\omega-2\Omega)t} \right] \vec{\epsilon}, \quad (\text{E.18})$$

where $\boldsymbol{\sigma}(\omega)$, $\boldsymbol{\sigma}^{+}(\omega)$ and $\boldsymbol{\sigma}^{-}(\omega)$ are the conductivity matrices corresponding to the frequencies ω , $\omega + 2\Omega$ and $\omega - 2\Omega$, given by:

$$\begin{aligned} \boldsymbol{\sigma}(\omega) &= -\frac{i}{\omega} (\mathbf{M}_{+} \mathbf{X}_{+} \mathbf{M}_{+} + \mathbf{M}_{-} \mathbf{X}_{-} \mathbf{M}_{-}), \\ \boldsymbol{\sigma}^{+}(\omega) &= -\frac{i}{\omega} \mathbf{M}_{-} \mathbf{X}_{-} \mathbf{M}_{+}, \\ \boldsymbol{\sigma}^{-}(\omega) &= -\frac{i}{\omega} \mathbf{M}_{+} \mathbf{X}_{+} \mathbf{M}_{-}. \end{aligned} \quad (\text{E.19})$$

E.1 Masless limit

In the massless case the fluctuations of the embedding function decouple from those of the gauge field $\delta\vec{c}$. Therefore, since we are interested in computing conductivities, we can concentrate in studying the equations for δc_x and δc_y . In order to write these equations in a more convenient form, let us define the following differential operators

$$\begin{aligned} \mathcal{O}_1 &\equiv \partial_t^2 + \frac{(r^4 - r_h^4)^2 (r_c^4 - r_h^4)}{\rho^4 (r_c^4 + r^4 - 2r_h^4)} \partial_r^2 - \frac{2(r^4 - r_h^4)(r_c^4 - r_h^4)}{r^2 (r_c^4 + r^4 - 2r_h^4)} \partial_t \partial_r + \\ &\quad \frac{4r(r_c^4 - r_h^4)}{(r_c^4 + r^4 - 2r_h^4)} \partial_t - \frac{2(r^4 - r_h^4)^2 (r_c^4 + r^4)}{r^5 (r_c^4 + r^4 - 2r_h^4)} \partial_r, \\ \mathcal{O}_2 &\equiv -2\partial_t + \frac{2(r^4 - r_h^4)(r_c^4 - r_h^4)}{\rho^2 (r_c^4 + r^4 - 2r_h^4)} \partial_r + \frac{4r(r^4 - r_h^4)}{r_c^4 + r^4 - 2r_h^4}. \end{aligned} \quad (\text{E.20})$$

Then, one can show that δc_x and δc_y satisfy the following system of coupled second-order differential equations

$$(\mathcal{O}_1 - \Omega^2) \delta c_x + \Omega \mathcal{O}_2 \delta c_y = 0, \quad (\mathcal{O}_1 - \Omega^2) \delta c_y - \Omega \mathcal{O}_2 \delta c_x = 0. \quad (\text{E.21})$$

To decouple these equations, let us consider the following complex combinations of δc_x and δc_y

$$\eta(t, r) \equiv \delta c_x(t, r) + i \delta c_y(t, r), \quad \tilde{\eta}(t, r) \equiv \delta c_x(t, r) - i \delta c_y(t, r). \quad (\text{E.22})$$

Notice that $\tilde{\eta}$ is not the complex conjugate of η since δc_x and δc_y are not necessarily real. It is straightforward to verify that the equations for η and $\tilde{\eta}$ are indeed decoupled and given by

$$(\mathcal{O}_1 - \Omega^2) \eta - i \Omega \mathcal{O}_2 \eta = 0, \quad (\mathcal{O}_1 - \Omega^2) \tilde{\eta} + i \Omega \mathcal{O}_2 \tilde{\eta} = 0. \quad (\text{E.23})$$

Let us now separate variables as

$$\eta(t, r) = \beta(r) e^{-i\omega t}, \quad \tilde{\eta}(t, r) = \tilde{\beta}(r) e^{-i\omega t}, \quad (\text{E.24})$$

for some frequency ω . Then, we obtain the following differential equations for β :

$$\begin{aligned} r(r^4 - r_c^4)(r^4 - r_h^4)^2 \beta'' = & -2(r^4 - r_h^4) \left[r^8 - r_c^4 r_h^4 + r^4(r_c^4 - r_h^4) - i r^3(r_c^4 - r_h^4)(\omega - \Omega) \right] \beta' - \\ & - r^5(\omega - \Omega) \left[4i r(r_c^4 - r_h^4) + r^4(\omega - \Omega) + (r_c^4 - 2r_h^4)(\omega - \Omega) \right] \beta. \end{aligned} \quad (\text{E.25})$$

The equation for $\tilde{\beta}$ is the same, but with $(\omega + \Omega)$ instead of $(\omega - \Omega)$. Then, remarkably, one can find the following general solutions

$$\begin{aligned} \beta(r) &= e^{i \frac{\Omega - \omega}{4r_h} \Lambda\left(\frac{r}{r_h}\right)} \left[A + B e^{-i \frac{\Omega - \omega}{2r_c} \Lambda\left(\frac{r}{r_c}\right)} \right], \\ \tilde{\beta}(r) &= e^{-i \frac{\Omega + \omega}{4r_h} \Lambda\left(\frac{r}{r_h}\right)} \left[\tilde{A} + \tilde{B} e^{i \frac{\Omega + \omega}{2r_c} \Lambda\left(\frac{r}{r_c}\right)} \right], \end{aligned} \quad (\text{E.26})$$

where Λ is the function defined in (D.10) and A, B, \tilde{A} and \tilde{B} are complex constants which are determined by imposing boundary conditions both at the IR and UV. First of all, we write the solutions we found in terms of the tortoise coordinates (τ, r_*) of (D.41). Actually, by inspecting the expression of η obtained from (E.26) one easily demonstrates that, in terms of the tortoise variables, it can be simply written as

$$\eta(\tau, r_*) = e^{\frac{\Omega}{4r_h} \Lambda\left(\frac{r}{r_h}\right)} \left[A e^{-i\omega(\tau+r_*)} + B e^{-2i\Omega r_*} e^{-i\omega(\tau-r_*)} \right] \quad (\text{E.27})$$

It is now clear that $\eta(\tau, r_*)$ is the superposition of ingoing and outgoing waves at the pseudohorizon. The infalling regularity condition requires that B vanishes. Then, writing η in our original (t, r) coordinates, we have

$$\eta(t, r) = A e^{-i \frac{\omega - \Omega}{4r_h} \Lambda\left(\frac{r}{r_h}\right)} e^{-i\omega t}. \quad (\text{E.28})$$

We can proceed similarly with $\tilde{\eta}$ and conclude that we should require that $\tilde{B} = 0$. Therefore

$$\tilde{\eta}(t, r) = \tilde{A} e^{-i \frac{\omega+\Omega}{4r_h} \Lambda\left(\frac{r}{r_h}\right)} e^{-i\omega t}. \quad (\text{E.29})$$

Therefore, we obtain that the fluctuations δc_x and δc_y regular at the pseudohorizon are

$$\begin{aligned} \delta c_x(t, r) &= \frac{1}{2} \left[A e^{-i \frac{\omega-\Omega}{4r_h} \Lambda\left(\frac{r}{r_h}\right)} + \tilde{A} e^{-i \frac{\omega+\Omega}{4r_h} \Lambda\left(\frac{r}{r_h}\right)} \right] e^{-i\omega t}, \\ \delta c_y(t, r) &= \frac{1}{2i} \left[A e^{-i \frac{\omega-\Omega}{4r_h} \Lambda\left(\frac{r}{r_h}\right)} - \tilde{A} e^{-i \frac{\omega+\Omega}{4r_h} \Lambda\left(\frac{r}{r_h}\right)} \right] e^{-i\omega t}. \end{aligned} \quad (\text{E.30})$$

Let us now impose the boundary conditions at the UV. To fulfil the UV boundary condition (E.10) we sum two solutions of the form (E.30) with frequencies $\omega_+ = \omega + \Omega$ and $\omega_- = \omega - \Omega$. Let A_{\pm} and \tilde{A}_{\pm} denote the constants in (E.30) with frequency ω_{\pm} . From the leading UV terms we get that, in order to satisfy the boundary condition (E.15), the constants A_{\pm} and \tilde{A}_{\pm} must be related to ϵ_x and ϵ_y as:

$$A_+ = -\frac{i}{\omega} (\epsilon_x + i\epsilon_y), \quad \tilde{A}_- = -\frac{i}{\omega} (\epsilon_x - i\epsilon_y), \quad \tilde{A}_+ = A_- = 0. \quad (\text{E.31})$$

Moreover, from the analysis of the subleading UV terms we conclude that

$$\vec{\beta}_{\pm}^{(1)} = \mathbf{M}_{\pm} \vec{\epsilon}. \quad (\text{E.32})$$

By comparing (E.32) and (E.17), we get that the matrices \mathbf{X}_{\pm} are given by:

$$\mathbf{X}_{\pm} = i\omega \mathbf{I}. \quad (\text{E.33})$$

Plugging these \mathbf{X}_{\pm} matrices in (E.20), we obtain the conductivity matrices in these massless case, namely

$$\boldsymbol{\sigma}(\omega) = \mathbf{I}, \quad \boldsymbol{\sigma}^+(\omega) = \boldsymbol{\sigma}^-(\omega) = 0, \quad (\text{E.34})$$

which is exactly the same result as the one found in [1] at zero temperature. As in the case of the non-linear current, here also the result confirms the expectations put forward in [12].

F Linearized Minkowski embeddings and meson spectrum

To study Minkowski embeddings is rather convenient to use cartesian coordinates (ρ, w) , defined as:

$$\rho = u \cos \theta, \quad w = u \sin \theta, \quad (\text{F.1})$$

where u is the isotropic coordinate defined in (A.5) and θ is the angle of (A.4). In these coordinates the embeddings are parameterized by functions $w = w(\rho)$ and the effective lagrangian is given by

$$\begin{aligned} \mathcal{L} \sim & \frac{\rho^2}{(\rho^2 + w^2)^3} \left[(\rho^2 + w^2)^2 \left(u_h^4 - (\rho^2 + w^2)^2 \right)^2 |c'|^2 - \Omega^2 (\rho^2 + w^2)^4 \text{Re}\{c\bar{c}'\}^2 + \right. \\ & \left. + \left((\rho^2 + w^2)^2 + u_h^4 \right) (w'^2 + 1) \left(\left(u_h^4 - (\rho^2 + w^2)^2 \right)^2 - \Omega^2 (\rho^2 + w^2)^2 |c|^2 \right) \right]^{1/2}, \end{aligned} \quad (\text{F.2})$$

where $u_h = r_h/\sqrt{2}$ and now the primes denote derivatives with respect to ρ . Let us consider the case in which the gauge field $c(\rho)$ vanishes, and let $\tilde{w} = \tilde{w}(\rho)$ denote the Minkowski

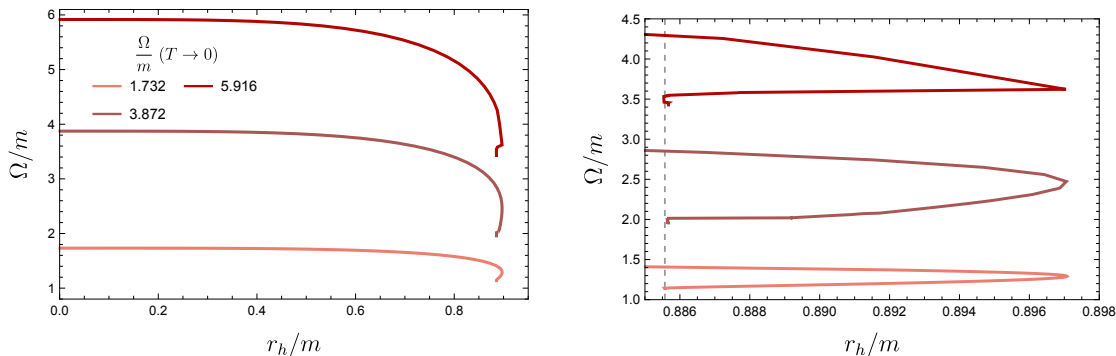


Figure 13. Ω/m variation with r_h/m . The right figure shows the endpoint of the curves. Both of them are bivaluated between $r_h/m = 0.8855$ to $r_h = 0.8897$, and stop for $r_h/m = 0.8855$.

embedding function in such case. It can be obtained by solving the equation of motion of the Lagrange density $\tilde{\mathcal{L}} = \mathcal{L}(c = 0)$

$$\tilde{\mathcal{L}} \sim \frac{\rho^2(u_h^4 - (\rho^2 + \tilde{w}^2)^2)}{(\rho^2 + \tilde{w}^2)^3} \sqrt{[(\rho^2 + \tilde{w}^2)^2 + u_h^2][\tilde{w}'^2 + 1]}. \quad (\text{F.3})$$

Let us next suppose that we perturb around the $c = 0$ solution by making $c \rightarrow \delta c$ and $w \rightarrow \tilde{w} + \delta w$ in the equations of motion derived from the Lagrangian density (F.2). It is easy to see that, at first order in the variations, the equation for δc reads

$$\partial_\rho \left(\frac{\rho^2 (u_h^4 - (\rho^2 + \tilde{w}^2)^2)}{(\rho^2 + \tilde{w}^2) \sqrt{((\rho^2 + \tilde{w}^2)^2 + u_h^4) (\tilde{w}'^2 + 1)}} \delta c' \right) + \frac{\rho^2 \Omega^2 \sqrt{((\rho^2 + \tilde{w}^2)^2 + u_h^4)}}{(\rho^2 + \tilde{w}^2) (u_h^4 - (\rho^2 + \tilde{w}^2)^2) \sqrt{\tilde{w}'^2 + 1}} \delta c = 0. \quad (\text{F.4})$$

To obtain the resonant frequencies of the mesonic Floquet condensates we integrate (F.4) and find the solutions that are regular at $\rho = 0$ and such that $E = 0$ when we reach $j = 0$ after each critical driving frequency Ω_c/m (see the lower plot in figure 6). This last condition is only possible when the frequency Ω/m takes values in a discrete set (which depends on the horizon radius r_h). For $r_h/m = 0$, i.e. at zero temperature, this sequence of frequencies can be obtained analytically and is given by [1]

$$\frac{\Omega}{m} \Big|_{T=0} = 2 \sqrt{\left(n + \frac{1}{2}\right) \left(n + \frac{3}{2}\right)}, \quad (n = 0, 1, 2, \dots), \quad (\text{F.5})$$

which are just the masses of the vector mesons of the supersymmetric D3-D5 model [45]. For $r_h/m \neq 0$ the masses of these mesonic states decrease as r_h/m grows. At some value of r_h/m they cease to exist (see figure 13), as the mere Minkowski embedding themselves do (see section 3). This behavior is dual to the meson melting phenomenon, as discussed in [44].

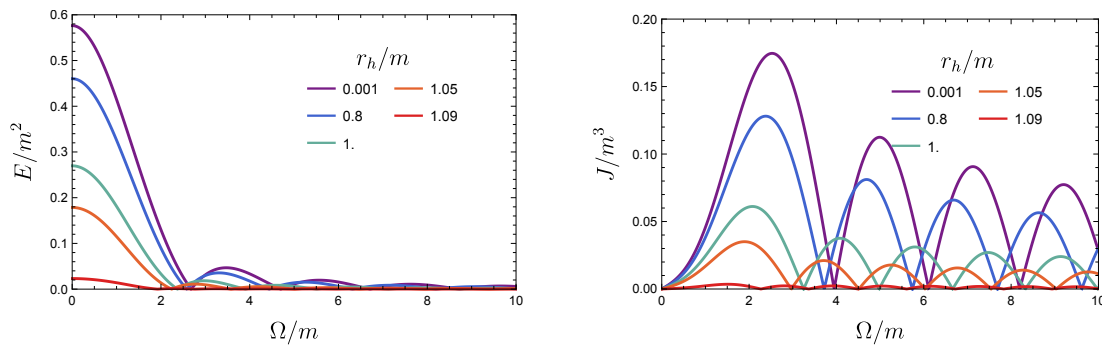


Figure 14. Electric field and current of the critical embeddings versus driving frequency, for different values of r_h in the D3/D7 system. The structure is mainly the same as the one found for the D3/D5 case. Here the maximum temperature for the Minkowski embeddings is slightly higher, while the height of the lobes is suppressed faster as one increases the driving frequency.

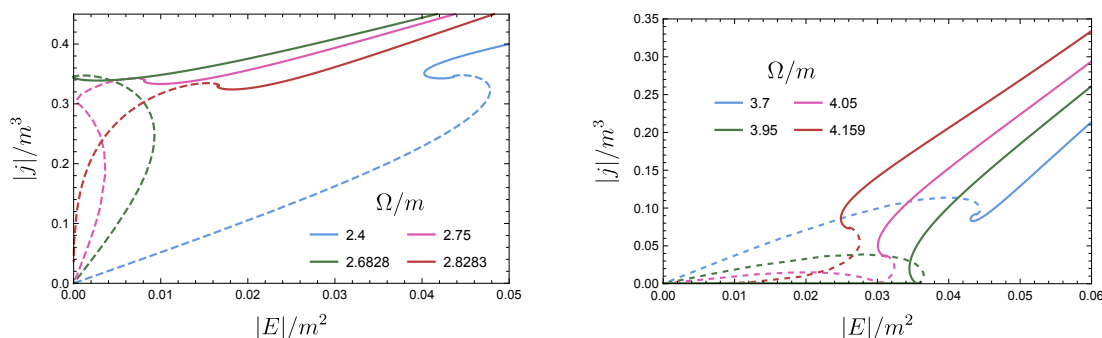


Figure 15. Electric current $|j|/m^3$ versus electric field $|E|/m^2$ for $r_h/m = 0.001$. The solid curves represent the insulator (Minkowski) phase and the dashed curves the conductive (BH) phase. The driving frequency is fixed to some $\Omega/m < \Omega_c/m$ (blue), $\Omega/m = \Omega_c/m$ (green), $\Omega_c/m < \Omega/m < \Omega_m/m$ (pink) and $\Omega/m = \Omega_m/m$ (red). The curves the left, with $\Omega \sim 2.68$ scan the region close to the Floquet vector meson condensates and were obtained in [10]. On the right, for $\Omega \sim 3.95$ we do the same around the first Floquet suppression point.

G Phase space structure for the D3/D7 system

It is worth mentioning that the existence of these Floquet suppression points is not restricted to the D3/D5 system. In figure 14 we reproduce the lobe structure for the D3/D7 system, which is analogous to the one found in figure 3 for D3/D5. The $r_h \rightarrow 0$ limit for the electric field plot coincides, of course, with the one studied in [10].

We find again a set of points where the induced current vanishes while the electric field is close to its maximum value within the lobe. This seems to indicate the presence of a range of frequencies for which, in Minkowski embeddings, $|j| = 0$ with $|E| \neq 0$, ranging from the critical frequency of the current $\Omega_{c,j}$ (c stands for critical) up to son maximum value $\Omega_{m,j}$ (m stands form meson).

The analytic computation of $\Omega_{m,j}$ in the $T = 0$ limit of the D3/D7 system is more complicated than the one corresponding to the D3/D5 intersection but it can, however, be obtained numerically. We have found that the Floquet suppression points first appear for $\Omega/m \in (3.950, 4.159)$, and plotted in figure 15 the modulus of the current and the electric

field for frequencies close or within that range. As anticipated, the similarity with the structure studied in [10] is quite obvious, and thus we conclude that a 3D diagram as that of figure 7 is also found when studying D3/D7 branes.

Open Access. This article is distributed under the terms of the Creative Commons Attribution License ([CC-BY 4.0](https://creativecommons.org/licenses/by/4.0/)), which permits any use, distribution and reproduction in any medium, provided the original author(s) and source are credited. SCOAP³ supports the goals of the International Year of Basic Sciences for Sustainable Development.

References

- [1] A. Garbayo, J. Mas and A.V. Ramallo, *Holographic Floquet states in low dimensions*, *JHEP* **10** (2020) 013 [[arXiv:2007.12115](https://arxiv.org/abs/2007.12115)] [[INSPIRE](#)].
- [2] M. Bukov, L. D'Alessio and A. Polkovnikov, *Universal high-frequency behavior of periodically driven systems: from dynamical stabilization to Floquet engineering*, *Adv. Phys.* **64** (2015) 139 [[arXiv:1407.4803](https://arxiv.org/abs/1407.4803)].
- [3] A. Eckardt, *Colloquium: Atomic quantum gases in periodically driven optical lattices*, *Rev. Mod. Phys.* **89** (2017) 011004 [[arXiv:1606.08041](https://arxiv.org/abs/1606.08041)] [[INSPIRE](#)].
- [4] P. Weinberg, M. Bukov, L. D'Alessio, A. Polkovnikov, S. Vajna and M. Kolodrubetz, *Adiabatic perturbation theory and geometry of periodically-driven systems*, *Phys. Rept.* **688** (2017) 1 [[arXiv:1606.02229](https://arxiv.org/abs/1606.02229)].
- [5] M. Holthaus, *Floquet engineering with quasienergy bands of periodically driven optical lattices*, *J. Phys. B* **49** (2016) 013001 [[arXiv:1510.09042](https://arxiv.org/abs/1510.09042)].
- [6] T. Oka and S. Kitamura, *Floquet Engineering of Quantum Materials*, *Ann. Rev. Condens. Matter Phys.* **10** (2019) 387 [[arXiv:1804.03212](https://arxiv.org/abs/1804.03212)].
- [7] U.D. Giovannini and H. Hubener, *Floquet analysis of excitations in materials*, *J. Phys. Materials* **3** (2019) 012001 [[arXiv:1907.00614](https://arxiv.org/abs/1907.00614)].
- [8] M.S. Rudner and N.H. Lindner, *The Floquet Engineer's Handbook*, [arXiv:2003.08252](https://arxiv.org/abs/2003.08252).
- [9] K. Hashimoto, S. Kinoshita, K. Murata and T. Oka, *Holographic Floquet states I: a strongly coupled Weyl semimetal*, *JHEP* **05** (2017) 127 [[arXiv:1611.03702](https://arxiv.org/abs/1611.03702)] [[INSPIRE](#)].
- [10] B. Chen, L. Chen, P.-x. Hao and J. Long, *On the Mutual Information in Conformal Field Theory*, *JHEP* **06** (2017) 096 [[arXiv:1704.03692](https://arxiv.org/abs/1704.03692)] [[INSPIRE](#)].
- [11] A. Karch and A. O'Bannon, *Metallic AdS/CFT*, *JHEP* **09** (2007) 024 [[arXiv:0705.3870](https://arxiv.org/abs/0705.3870)] [[INSPIRE](#)].
- [12] A. Karch and S.L. Sondhi, *Non-linear, Finite Frequency Quantum Critical Transport from AdS/CFT*, *JHEP* **01** (2011) 149 [[arXiv:1008.4134](https://arxiv.org/abs/1008.4134)] [[INSPIRE](#)].
- [13] O. DeWolfe, D.Z. Freedman and H. Ooguri, *Holography and defect conformal field theories*, *Phys. Rev. D* **66** (2002) 025009 [[hep-th/0111135](https://arxiv.org/abs/hep-th/0111135)] [[INSPIRE](#)].
- [14] A. Karch and E. Katz, *Adding flavor to AdS/CFT*, *JHEP* **06** (2002) 043 [[hep-th/0205236](https://arxiv.org/abs/hep-th/0205236)] [[INSPIRE](#)].
- [15] J. Erdmenger, Z. Guralnik and I. Kirsch, *Four-dimensional superconformal theories with interacting boundaries or defects*, *Phys. Rev. D* **66** (2002) 025020 [[hep-th/0203020](https://arxiv.org/abs/hep-th/0203020)] [[INSPIRE](#)].

- [16] J. Sonner and A.G. Green, *Hawking Radiation and Non-equilibrium Quantum Critical Current Noise*, *Phys. Rev. Lett.* **109** (2012) 091601 [[arXiv:1203.4908](#)] [[INSPIRE](#)].
- [17] S. Nakamura and H. Ooguri, *Out of Equilibrium Temperature from Holography*, *Phys. Rev. D* **88** (2013) 126003 [[arXiv:1309.4089](#)] [[INSPIRE](#)].
- [18] J. Mas, J.P. Shock and J. Tarrio, *Holographic Spectral Functions in Metallic AdS/CFT*, *JHEP* **09** (2009) 032 [[arXiv:0904.3905](#)] [[INSPIRE](#)].
- [19] K.-Y. Kim, J.P. Shock and J. Tarrio, *The open string membrane paradigm with external electromagnetic fields*, *JHEP* **06** (2011) 017 [[arXiv:1103.4581](#)] [[INSPIRE](#)].
- [20] T. Ishii and K. Murata, *Floquet superconductor in holography*, *Phys. Rev. D* **98** (2018) 126005 [[arXiv:1804.06785](#)] [[INSPIRE](#)].
- [21] J. Erdmenger, N. Evans, I. Kirsch and E. Threlfall, *Mesons in Gauge/Gravity Duals — A Review*, *Eur. Phys. J. A* **35** (2008) 81 [[arXiv:0711.4467](#)] [[INSPIRE](#)].
- [22] A. Kundu, *Steady States, Thermal Physics, and Holography*, *Adv. High Energy Phys.* **2019** (2019) 2635917 [[INSPIRE](#)].
- [23] A. Karch, A. O’Bannon and E. Thompson, *The Stress-Energy Tensor of Flavor Fields from AdS/CFT*, *JHEP* **04** (2009) 021 [[arXiv:0812.3629](#)] [[INSPIRE](#)].
- [24] S.A. Hartnoll, P.K. Kovtun, M. Muller and S. Sachdev, *Theory of the Nernst effect near quantum phase transitions in condensed matter, and in dyonic black holes*, *Phys. Rev. B* **76** (2007) 144502 [[arXiv:0706.3215](#)] [[INSPIRE](#)].
- [25] T. Oka and H. Aoki, *Photovoltaic Hall effect in graphene*, *Phys. Rev. B* **79** (2009) 081406 [[arXiv:0807.4767](#)].
- [26] T. Oka and H. Aoki, *All Optical Measurement Proposed for the Photovoltaic Hall Effect*, *J. Phys. Conf. Ser.* **334** (2011) 012060 [[arXiv:1007.5399](#)].
- [27] H.-J. Schmidt, J. Schnack and M. Holthaus, *Periodic thermodynamics of the rabi model with circular polarization for arbitrary spin quantum numbers*, *Phys. Rev. E* **100** (2019) 042141 [[arXiv:1902.05814](#)].
- [28] O. Aharony, O. Bergman, D.L. Jafferis and J. Maldacena, *$N = 6$ superconformal Chern-Simons-matter theories, M2-branes and their gravity duals*, *JHEP* **10** (2008) 091 [[arXiv:0806.1218](#)] [[INSPIRE](#)].
- [29] S. Hohenegger and I. Kirsch, *A Note on the holography of Chern-Simons matter theories with flavour*, *JHEP* **04** (2009) 129 [[arXiv:0903.1730](#)] [[INSPIRE](#)].
- [30] D. Gaiotto and D.L. Jafferis, *Notes on adding D6 branes wrapping RP^3 in $AdS_4 \times CP^3$* , *JHEP* **11** (2012) 015 [[arXiv:0903.2175](#)] [[INSPIRE](#)].
- [31] N. Jokela, J. Mas, A.V. Ramallo and D. Zoakos, *Thermodynamics of the brane in Chern-Simons matter theories with flavor*, *JHEP* **02** (2013) 144 [[arXiv:1211.0630](#)] [[INSPIRE](#)].
- [32] E. Conde, H. Lin, J.M. Penin, A.V. Ramallo and D. Zoakos, *D3-D5 theories with unquenched flavors*, *Nucl. Phys. B* **914** (2017) 599 [[arXiv:1607.04998](#)] [[INSPIRE](#)].
- [33] J.M. Penin, A.V. Ramallo and D. Zoakos, *Anisotropic D3-D5 black holes with unquenched flavors*, *JHEP* **02** (2018) 139 [[arXiv:1710.00548](#)] [[INSPIRE](#)].
- [34] N. Jokela, J.M. Penín, A.V. Ramallo and D. Zoakos, *Gravity dual of a multilayer system*, *JHEP* **03** (2019) 064 [[arXiv:1901.02020](#)] [[INSPIRE](#)].

- [35] A. Garbayo, C. Hoyos, N. Jokela, J.M. Penín and A.V. Ramallo, *Flavored anisotropic black holes*, *JHEP* **10** (2022) 061 [[arXiv:2208.04958](#)] [[INSPIRE](#)].
- [36] C. Núñez, A. Paredes and A.V. Ramallo, *Unquenched Flavor in the Gauge/Gravity Correspondence*, *Adv. High Energy Phys.* **2010** (2010) 196714 [[arXiv:1002.1088](#)] [[INSPIRE](#)].
- [37] S.R. Das, T. Nishioka and T. Takayanagi, *Probe Branes, Time-dependent Couplings and Thermalization in AdS/CFT*, *JHEP* **07** (2010) 071 [[arXiv:1005.3348](#)] [[INSPIRE](#)].
- [38] C. Hoyos, T. Nishioka and A. O’Bannon, *A Chiral Magnetic Effect from AdS/CFT with Flavor*, *JHEP* **10** (2011) 084 [[arXiv:1106.4030](#)] [[INSPIRE](#)].
- [39] P. Glorioso, M. Crossley and H. Liu, *A prescription for holographic Schwinger-Keldysh contour in non-equilibrium systems*, [arXiv:1812.08785](#) [[INSPIRE](#)].
- [40] C. Jana, R. Loganayagam and M. Rangamani, *Open quantum systems and Schwinger-Keldysh holograms*, *JHEP* **07** (2020) 242 [[arXiv:2004.02888](#)] [[INSPIRE](#)].
- [41] A. Karch, A. O’Bannon and K. Skenderis, *Holographic renormalization of probe D-branes in AdS/CFT*, *JHEP* **04** (2006) 015 [[hep-th/0512125](#)] [[INSPIRE](#)].
- [42] A. Kundu and S. Kundu, *Steady-state Physics, Effective Temperature Dynamics in Holography*, *Phys. Rev. D* **91** (2015) 046004 [[arXiv:1307.6607](#)] [[INSPIRE](#)].
- [43] A. Banerjee, A. Kundu and S. Kundu, *Flavour Fields in Steady State: Stress Tensor and Free Energy*, *JHEP* **02** (2016) 102 [[arXiv:1512.05472](#)] [[INSPIRE](#)].
- [44] D. Mateos, R.C. Myers and R.M. Thomson, *Thermodynamics of the brane*, *JHEP* **05** (2007) 067 [[hep-th/0701132](#)] [[INSPIRE](#)].
- [45] D. Areal and A.V. Ramallo, *Open string modes at brane intersections*, *JHEP* **04** (2006) 037 [[hep-th/0602174](#)] [[INSPIRE](#)].